Cell Reports
Physical Science

CellPress
OPEN ACCESS

Article

High-power iontronics enabled by nanoconfined ion dynamics

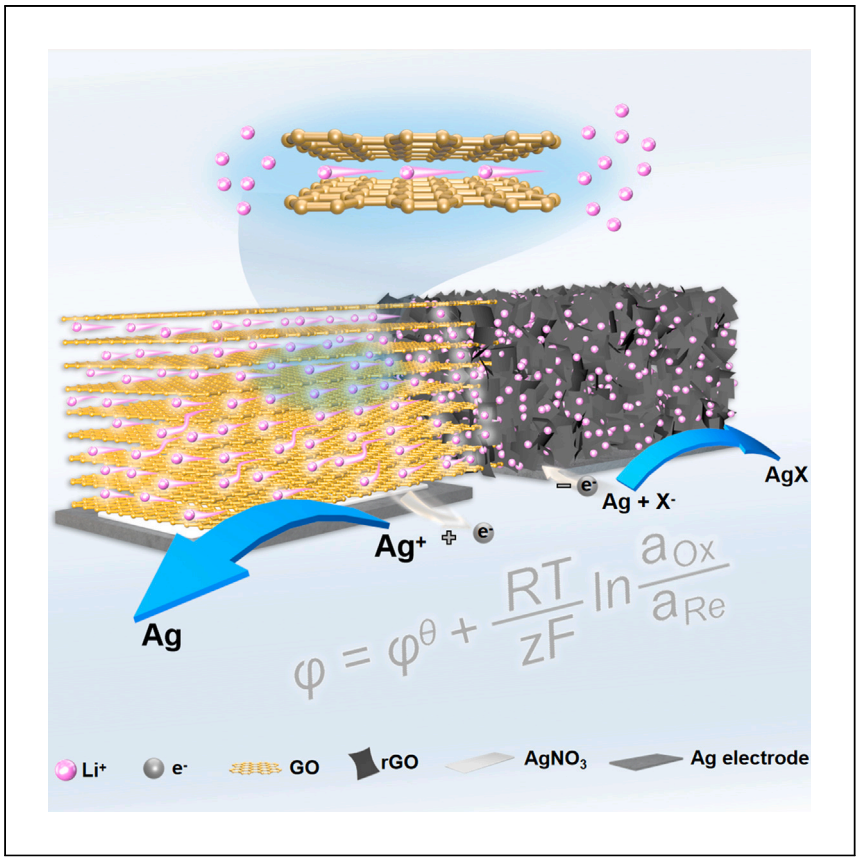

By coupling fine-tuned interfacial Ag/Ag^+ redox reactions with efficient cation transport in graphene oxide (GO) nanoconfined channels, Peng et al. design an all-solid, ultrathin, and high-power iontronic power source. It can also be printed over a large area and self-charged, making it ideal for wearable electronics.

Puguang Peng, Feiyao Yang, Xiang Li, Shaoxin Li, Zhonglin Wang, Di Wei

zhong.wang@mse.gatech.edu (Z.W.)
weidi@binn.cas.cn (D.W.)

Highlights

Interfacial Ag/Ag^+ redox reactions enhance the ion dynamics in nanoconfined GO

An all-solid, ultrathin, and high-power iontronic power source is developed

Pseudocapacitive process is responsible for the enhanced ion dynamics

Iontronics can be made via printing and self-charged by TENG for wide applications

Peng et al., Cell Reports Physical Science 5, 101824
February 21, 2024
https://doi.org/10.1016/j.xcrp.2024.101824

Please cite this article in press as: Peng et al., High-power iontronics enabled by nanoconfined ion dynamics, Cell Reports Physical Science (2024), https://doi.org/10.1016/j.xcrp.2024.101824

Cell Reports
Physical Science

CellPress
OPEN ACCESS

Article

High-power iontronics enabled by nanoconfined ion dynamics

Puguang Peng,[1,2] Feiyao Yang,[1] Xiang Li,[1,2] Shaoxin Li,[1,2] Zhonglin Wang,[1,3,*] and Di Wei[1,2,4,*]

SUMMARY

Tailoring ion dynamics within nanoconfined spaces presents a new approach for developing advanced iontronic devices. Using various nano-hierarchical materials with nanoconfined spaces can regulate anomalous ionic behaviors, but research on coupling interfacial reactions and ionic dynamics in nanoconfined spaces remains unclear, which limits their applications in energy harvesting. Here, we develop an ultrathin (~10.5 μm), solid-state, and high-power iontronic power source with an areal energy density of ~1.4 kWh m^{-2} and power density of ~16.07 kW m^{-2}. This is achieved by coupling fine-tuned interfacial Ag/Ag^{+} redox reactions with efficient cation transport in graphene oxide (GO) nanoconfined channels. The iontronics can also be printed over a large fractal area and be self-charged by a triboelectric nanogenerator, which is crucial for futuristic wearable electronics and neuronal-computer interfaces. This work provides a paradigm of coupling various redox reactions to expand the iontronic systems to wider prospective applications.

INTRODUCTION

Unlike macroscopic ion transport behavior, the ion transport process in the nanoconfined space could be regulated accurately like in biological systems.[1] This is due to the different ion interactions within different confined space limits.[2] The dynamics of ion transport follow the general physiochemical rules in a system with a diameter larger than 100 nm. In a confined system with a diameter between 2 and 100 nm, electrostatic forces will predominate, and the transport of ions is mainly regulated by the electrical double layer (EDL).[3,4] Furthermore, in a confined system with a diameter of less than 2 nm, the hydration and weak interaction forces (hydrogen bonding, van der Waals force, etc.) will play an increasingly important role in the regulation of ions and give rise to a range of anomalous ionic behaviors, such as EDL overlapping, ionic Coulombic blockade, superionic states, drastic changes in diffusion coefficients, ion-ion correlation, ultra-dense packing of ions, etc.[5–10] Meanwhile, the classical mechanical and thermodynamic equations, such as the Navier-Stokes equation, Kelvin equation, and Hertz-Knudsen equation, are challenged in a small-pore-size (<2 nm) system.[11,12] The charge attraction and steric effects in the nanoconfined space could restrict the disordered motion of ions, thus achieving the ordered superfluidity of ions like in biological membranes.[13] To overcome the physical limits of Moore's law faced by electronic integrated circuits under the von Neumann computing architecture, numerous iontronics, such as ionic memristors,[14] logic gated circuits,[15] neuromorphic diodes,[16,17] ionic gates,[18] ionic sieves,[19] ionic pressure sensors,[20,21] supercapacitors,[4] osmotic energy devices,[22–25] transistors,[6] and artificial synapses,[26] etc., based on nanoconfined ion dynamics, have been reported recently. It is vital to improve ion dynamics to enhance the iontronic performance, especially in the biologically compatible power sources.

[1]Beijing Institute of Nanoenergy and Nanosystems, Chinese Academy of Sciences, Beijing 101400, China

[2]School of Nanoscience and Engineering, University of Chinese Academy of Sciences, Beijing 100049, China

[3]School of Materials Science and Engineering, Georgia Institute of Technology, Atlanta, GA 30332, USA

[4]Lead contact

*Correspondence: zhong.wang@mse.gatech.edu (Z.W.), weidi@binn.cas.cn (D.W.)

https://doi.org/10.1016/j.xcrp.2024.101824

Materials with controlled and defined nanostructures play an essential role in regulating the motion of ions[27] and are used in the ionic-electronic coupling interface in iontronics, including 1D nanotubes,[12,28] 2D nanofluidic materials of graphene oxide (GO),[24] MoS_2,[22] MXene,[29] etc., and 3D nanoporous ionic conductive materials, including metal-organic frameworks (MOFs),[30] etc. The 2D nanofluidic material GO is particularly interesting due to its simple and economic preparation process that enables the construction of precise nanofluidic channels for efficient control of ion transport, avoiding the complicated E-beam or lithographic methods. The 2D nanofluidic channels of GO rebuilt/restacked by cost-effective printing/drop-casting methods are widely studied in various iontronics such as ionic sieving,[5] ionic diodes,[6] and osmotic power generation.[24,25] Although regulation of ions can be achieved by using such anomalous behaviors in nanoconfined structures, the dynamics of ions coupling with interfacial reactions is rarely studied. It should be noted that the interfacial faradic redox reactions introduce a chemical built-in electric field, and it influences the diffusion dynamics of ions in nanoconfined spaces.[31]

Here, an iontronic power source enabled by nanoconfined ion dynamics within 2D nanofluidic channels of GO was investigated. The directional ion migration from high concentration to low concentration could be generally transduced to electronic current at the surface of electrodes either by the redox reaction occurring at the electrodes (anodes and cathodes)[32] or by charge adsorption on the surface of electrodes without redox reactions.[33] The ionic-electronic coupling interface by simple charge adsorption in an osmotic power source is similar to the EDL supercapacitors, which usually have decent power density, but the energy density is related to the surface area.[34] When interfacial redox reactions are introduced, the energy density could be boosted analogous to the pseudocapacitors.[34,35] In this work, GO-based junctions between the Ag electrodes were constructed to transport Li^+ cations, and fine-tuned Ag/Ag^+ redox reactions were introduced at the electrode interface. GO can expand the translational degrees of freedom for cation transport, engendering unusual ion dynamics. The Li^+ cations were efficiently transported through 2D nanofluidic channels of GO driven by the salinity gradient. For $AgNO_3$ dispersed in the nanoconfined GO channels, Ag^+ would be replaced by Li^+, and the process was recorded by the *in situ* Fourier transform infrared spectroscopy (FTIR), where the transition peaks of NO^{3-} in FTIR moved to high wave numbers under polarization by the diffused Li^+. In addition, the formation of Li-N bonds was observed by X-ray photoelectron spectroscopy (XPS), and both the $LiNO_3$ and reduced Ag metal were formed, as evidenced by X-ray Diffraction (XRD). It revealed that the fast dynamics of Li^+ transport were coupled with the redox reaction of $Ag^+ + e^- \rightarrow Ag$. Both the interfacial dynamic characterization through calculations via cyclic voltammetric (CV) and 3D Bode analysis showed a finite diffusion-controlled property, which demonstrated the pseudocapacitance characteristics. The introduced Ag/Ag^+ interfacial redox reactions within the ionic-electronic coupling interface could enhance the ion diffusion dynamics and boost the open circuit voltage ($V_{oc} = E_{diff} + E_{redox}$) of the iontronic power source, which was composed of the diffusion potential (E_{diff}) generated from the pure salinity gradient and the redox potential (E_{redox}) from redox reactions.[22,36,37] The high-power iontronics could be printed in fully solid-state form and reached an areal energy density of ~1.4 kWh m^{-2} with a power density of ~16.07 kW m^{-2}, which are beyond those of lithium thin-film batteries and supercapacitors, respectively. In addition, integrated with a triboelectric nanogenerator (TENG), it could form a self-charging conformable triboiontronic device. Such a safe, planar, and ultrathin (~10.5 μm) iontronic power source could also be printed on any insulating substrate (plastics, paper, etc.) or integrated into a printed circuit board (PCB) on a large scale. It could be cut to fit a variety of electronics; for example, two cells in

Please cite this article in press as: Peng et al., High-power iontronics enabled by nanoconfined ion dynamics, Cell Reports Physical Science (2024), https://doi.org/10.1016/j.xcrp.2024.101824

series (with a total area of 0.12 cm^2) could power a calculator, and one cell with an area of 0.4 cm^2 could drive conformable sensors for monitoring temperature in the environment or human body. The fractal printable design of a Peano curve was used to further increase the length of the power source in a finite area to increase the short-circuit current (I_{sc}) to 12 mA, which could power a liquid crystal display that has higher current demands. Such fractal printable iontronics without toxic electrolytes could make osmotic power economically viable to broaden its applications, especially in futuristic wearable or implantable devices in neuron-computer interfaces that require ultrathin and safe energy sources. In addition, the nanoconfined ion dynamics could be also applied to other redox reactions and could be expanded to a wide range of prospective applications.

RESULTS AND DISCUSSION

The nanoconfined ion dynamics within 2D nanofluidic channels

A simple device was designed to study the correlation between ion dynamics and the built-in electric field in the 2D nanofluidic channels of GO. As shown in Figure 1A, two ion reservoirs with a size of 5 × 5 × 10 mm each, had asymmetric ion concentrations, marked C_1 and C_2, with a liquid volume of 200 μL and were connected by GO films. GO was chosen for its surface rich in functional groups (-COOH, -OH, -O-, etc.; Figure S1A) with large negative charges (zeta potential of −60 mV; Figure S1B), allowing fast unidirectional transport of cations in a horizontal direction to achieve high osmotic power. It is also possible to rapidly obtain 2D nanofluidic channels with confined structures by coating or printing of GO inks (Figures 1B, S1C, and S1D). Here, a GO film with a length of 4.98 mm, width of 2.01 mm, and height of ~5 μm was fabricated (Figures S1E–S1G), and the average layer spacing of the GO flakes shown by XRD was about 7.87 Å (Figure S2A). The hydrophilic functional groups on the GO surface would cause it to be highly susceptible to hydrogen bonds for swelling due to absorption of aqueous solutions (Figure S2A). Therefore, acrylic tape was used to compact the GO film, and the layer spacing was only increased by 1.01 Å after immersion in water for 5 min (Figure S2B). The real ionic diffusion area could be calculated as 1.56 × 10^{-8} m^2, as discussed in Note S1.

To choose a suitable cation in this study, a linear-scan voltammetric test from −1 to 1 V was used to determine the current-voltage (I-V) responses of different salt solutions of LiCl, NaCl, KCl, and $CaCl_2$ in the two ion reservoirs with equal concentrations (0.1 M), as shown in Figure 1C. All curves were linear, so Ohm's law could be used to estimate the ohmic conductivity (G) for each type of cation diffused through GO.[38] The G value increased from 11.05 μS for $CaCl_2$ (blue line), 22.83 μS for KCl (red line), and 37.32 μS for NaCl (yellow line) to 72.85 μS for LiCl (green line), respectively, showing the highest conductivity for Li^+ (Figures 1C and 1D). The conventional osmotic power source generates its current from the Gibbs free energy converted from net ion diffusion during the exchange of asymmetric ionic distribution at the ionic-electronic interface.[22,23,37] The V_{oc} of the iontronic power source should originate from both the osmotic diffusion part and the Faraday redox part shown in Note S2 and Figure 1E. The measured voltage might mainly come from the E_{redox} without the ion-selective membrane, and this did not count the mixed Gibbs free energy from diffusion as shown in Figures S3A–S3C. Therefore, the synergy of E_{diff} and E_{redox} is essential for the total energy of the iontronic power source. As shown in Figures 1F and S4A–S4F, the progressively increased t_+ values were obtained without any applied bias when the salinity gradients changed from 10^0 to 10^6, which was also in agreement with the results observed in previous literature.[22,23] Fick's first law was also used to analyze the ion dynamics in GO and showed a tendency of

Please cite this article in press as: Peng et al., High-power iontronics enabled by nanoconfined ion dynamics, Cell Reports Physical Science (2024), https://doi.org/10.1016/j.xcrp.2024.101824

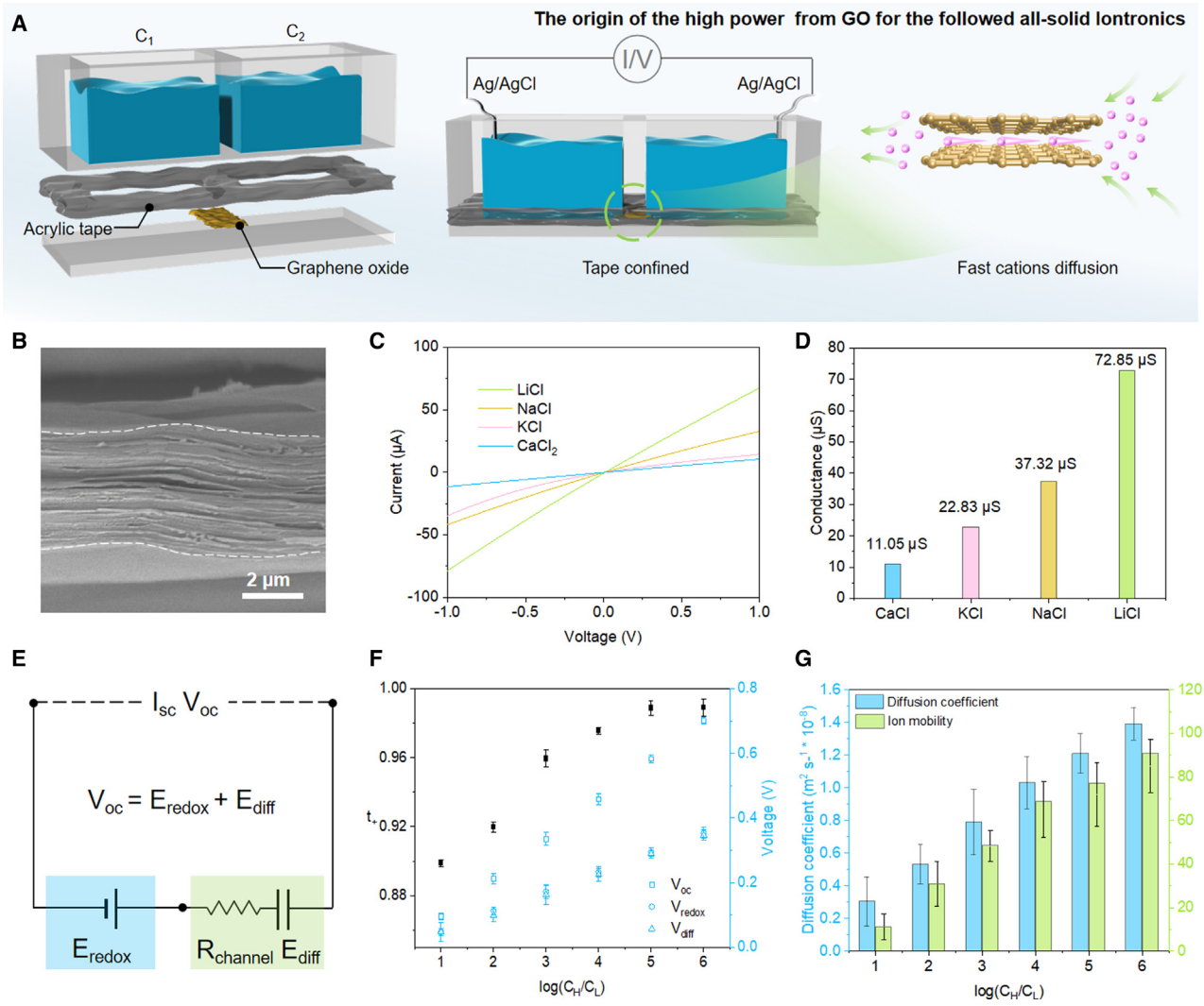

Figure 1. The ion dynamics within 2D nanofluidic channels of GO

(A) Schematic of the liquid system for ion diffusion and energy conversion.

(B) SEM photo of the GO film.

(C) I-V curve data without the salinity gradient of LiCl, NaCl, KCl, and $CaCl_2$. The concentration of each solution is 0.1 M.

(D) Ohmic conductance value as a function of types of cations.

(E) Diagram showing the contributions of different parts to the V_{oc} of the iontronic power source.

(F) t_+ and voltage contributions of different parts as a function of the salinity gradients.

(G) The calculated diffusion coefficient at different gradients.

increasing diffusion coefficient from 3.03×10^{-7} to 13.91×10^{-7} m^2 s^{-1} for Li^+ at different salinity gradients (Note S3; Figure 1G). In addition, the mobility of Li^+ in the nanofluidic channels of GO was also derived by Einstein's relational equation (Note S4; Figure S5), and the calculated range of Li^+ mobility with different salinity gradients is shown in Figure 1G (from 1.02×10^{-7} to 9.06×10^{-7} m^2 V^{-1} s^{-1}), which was almost corresponding to the calculated value of the diffusion coefficient. The built-in electric field on which we focus in this paper is different from the externally applied electric field, and it arises from the E_{redox} and charge redistribution at the ionic-electronic interface.[31,39,40] In nanoconfined spaces, some phenomena, such as ions desolvation,[41] concentration depolarization,[42,43] and the Debye layer overlapping, might interfere with ion diffusion. However, the ion-selective 2D nanofluidic

Please cite this article in press as: Peng et al., High-power iontronics enabled by nanoconfined ion dynamics, Cell Reports Physical Science (2024), https://doi.org/10.1016/j.xcrp.2024.101824

channels with the enhancement of a built-in electric field would generally lead to an increase in ion dynamics to promote the iontronic power.

All-solid-state high-power iontronics by coupling fine-tuned redox reactions

Cations within 2D nanofluidic channels of GO could be effectively driven by humidity in air[11,44] (Note S5; Figures S6A and S6B). The reduced graphene oxide (rGO), that reduced by L-ascorbic acid (LAA), formed porous structures with increased surface area and was used as an ionic reservoir for Li^+ cations (Figures S7A–S7D). It also had good conductivity (~0.25 S m^{-1}), which is helpful to improve the overall device performance (Figures S8A–S8B). The solid-state iontronic power source is shown in Figure 2A, with dimensions provided in Figures S9A–S9D; the Ag electrodes were first screen printed on a polyethylene terephthalate (PET) film to act as charge collectors. Solutions of GO (5 mg mL^{-1}) and $AgNO_3$ (1 mol L^{-1}) were drop cast and dried sequentially on the cathode side of the charge collector, followed by coating the anode side of the charge collector with rGO (5 mg mL^{-1}) containing lithium halide (LiX; 1 mol L^{-1}, where X = Cl^-, Br^-, I^-), overlapping to form a GO and rGO junction. By fine-tuning the redox reactions, the direction of the built-in electric field and the direction of the salinity gradient could be coordinated. The Ag/Ag^+ redox reactions were designed at the ionic-electronic interface to couple the salinity gradient of Li^+. The V_{oc} of Ag/$AgNO_3$-GO/LiX-rGO/Ag could be kept around 1.2 V for LiI, 0.95 V for LiBr, and 0.8V for LiCl under 40% relative humidity (RH; Beijing, 25°C), which are higher values than the respective values of 0.95 V, 0.73 V, and 0.58 V predicted by the Nernst equation. The extra voltage may come from the E_{diff} of salinity gradients, which was estimated to be ~10^6–10^7 (Figure 2B; Note S6). The I-V response of Ag/$AgNO_3$-GO/LiI-rGO/Ag was further verified under each RH, as shown in Figure 2C. It was found that the increase in RH was positively correlated with the I_{sc} but negatively correlated with the V_{oc} (Figure 2D). Under higher RH, the increase in I_{sc} might come from the reduced internal resistance within 2D nanofluidic channels of GO, and the decrease in V_{oc} may be caused by the rapidly diffusing equilibration of the ions. However, the voltage could be maintained around the value predicted the by Nernst equation even under a high RH of 80%, which may be due to the redox reaction that could form a chemical built-in electric field to cause continuous charge redistribution for a stable voltage output. The E_{diff} from Li^+ gradients may function as a switch in our iontronic power, as the V_{oc} was 0 V in the glovebox with extraordinarily low humidity (H_2O < 10 ppm; Figure S10A), and the voltage could be maintained for more than 300 h under a RH of 10% (Figure S10B). This also provides a method to overcome the intrinsic challenge for all batteries, self-discharging, which happens as soon as the battery is assembled, by keeping our iontronic power source under the extraordinary low humidity conditions. Therefore, a RH of 80% was used as the optimal condition to perform electrochemical characterization of the iontronics that contained different anions. The obtained V_{oc} values of Ag/$AgNO_3$-GO/LiX-rGO/Ag were 0.595 V, 0.738 V, and 0.963 V for LiCl, LiBr, and LiI, respectively, which could perfectly match the theoretically calculated values from the Nernst equation (Figure 2E). On the other hand, the I_{sc} also followed the same increasing tendency from ~0.4 mA to ~0.5 mA and to ~0.8 mA for the corresponding iontronic power sources with X = Cl^-, Br^-, and I^-, and the maximum areal specific power density was calculated to be up to 245.64 mW cm^{-2}, 661.74 mW cm^{-2}, and 1,607.14 mW cm^{-2}, respectively (Figure 2F; Note S7). All tests were repeated more than three times, and the corresponding sample-to-sample variations are shown in Figure S11. This may be caused by the redox reaction-enhanced, built-in electric field that facilitates the ion diffusion in GO. Compared with the most recent progress of the osmotic power sources based on the nanoconfined enhancement (Table S1), a maximum areal power density up to 1,607.14 mW cm^{-2} was

CellPress OPEN ACCESS

Cell Reports Physical Science Article

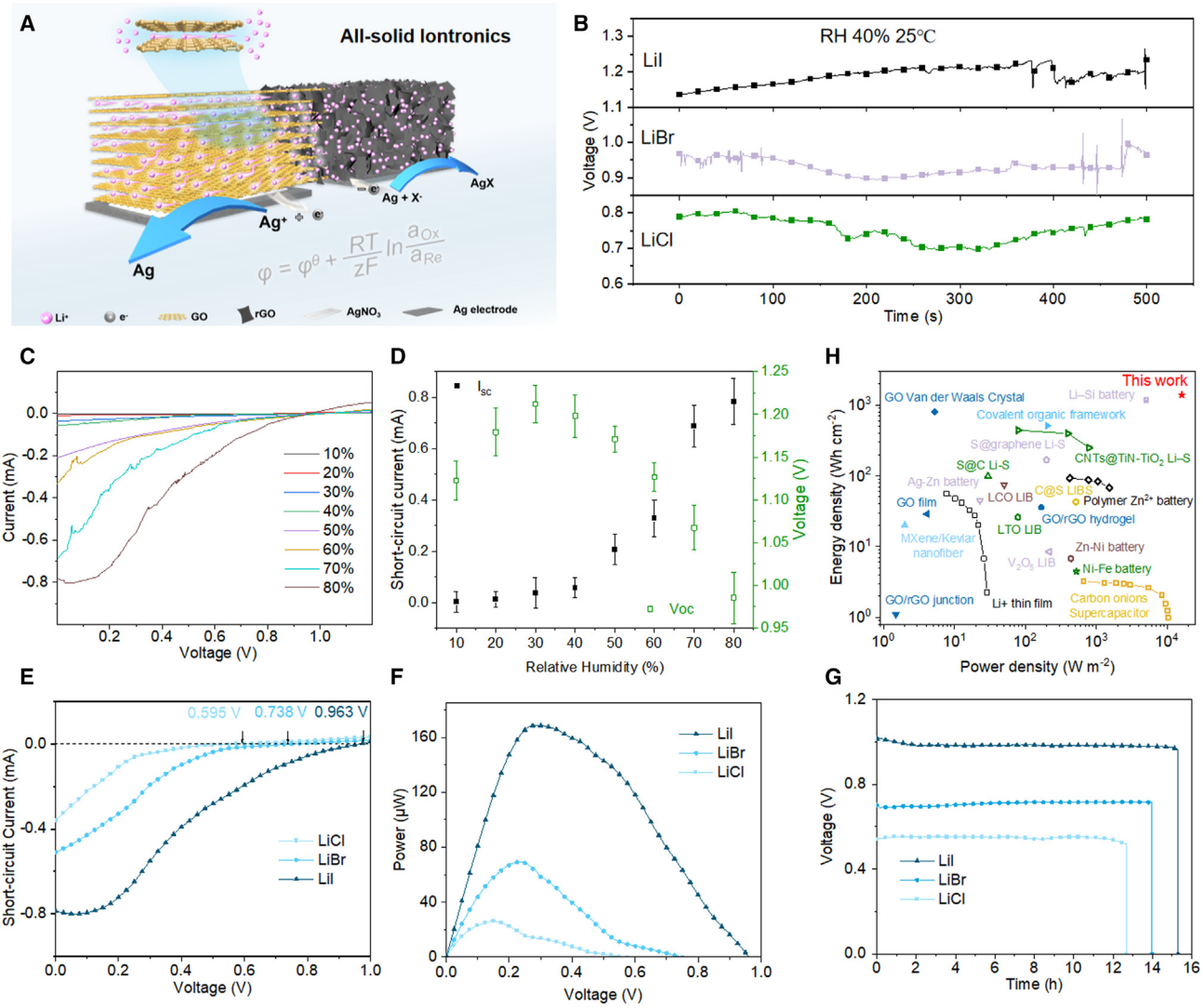

Figure 2. All-solid-state iontronic power source with redox couple in nanochannels

(A) Schematic of the iontronics and their mechanism.

(B) Long-time V_{oc} test for the iontronic power source loaded with different salts in rGO under an RH of 40%.

(C and D) I-V characteristics (C) and plots (D) of I_{sc} and V_{oc} of the Ag/$AgNO_3$-GO/LiI-rGO/Ag at various levels of RH.

(E) I-V characteristics of the iontronic power source loaded with different salts in rGO.

(F) Corresponding power densities of the osmotic power sources.

(G) Corresponding discharge curves of the iontronic power sources at 1 μA.

(H) Comparison of energy and power density of Ag/$AgNO_3$-GO/LiI-rGO/Ag in the Ragone plot (data for other power sources were collected from Table S1).

obtained from Ag/$AgNO_3$-GO/LiI-rGO/Ag, which exceeded the goal of making salinity gradient power economically viable (up to 0.5 mW cm^{-2}).[39]

Most osmotic power sources reported so far are kinds of energy harvesting methods rather than energy storage approaches due to the requirement of ionic reservoirs to maintain ion gradients; thus, it is difficult for them to keep stable voltage or generate high ionic current in a given volume. By using rGO as a cation reservoir and introducing interfacial redox reactions, the chronopotential test showed that our iontronic power source was able to discharge stably at around 0.94 V for 15 h at a

Please cite this article in press as: Peng et al., High-power iontronics enabled by nanoconfined ion dynamics, Cell Reports Physical Science (2024), https://doi.org/10.1016/j.xcrp.2024.101824

current of 1 μA (Figure 2G) with an areal energy density of 139.16 mWh cm^{-2}. In addition, the energy density was calculated as 70.83 mWh cm^{-2} for Ag/$AgNO_3$-GO/LiBr-rGO/Ag and 49.36 mWh cm^{-3} for Ag/$AgNO_3$-GO/LiCl-rGO/Ag (Figure 2G). Both the energy and power of them were not as high as that of Ag/$AgNO_3$-GO/LiI-rGO/Ag, probably due to the limitation of their lower voltage. It proved that all iontronic power sources with different LiXs followed the Nernst equation perfectly. The output (in mW cm^{-2} and mWh cm^{-2}) of different osmotic power sources and batteries with various materials are compared in Table S1, and our iontronic power source generated by far the highest areal power and energy density among them. Such energy density even exceeds that of lithium thin-film batteries, as shown in the Ragone plot in Figure 2H. Considering the reversibility of redox reactions, $Ag^+ + e^- \rightleftharpoons Ag$ and $Ag + I^- \rightleftharpoons AgI + e^-$ were selected as electrode pairs.

Cations could be generally transported effectively within 2D nanofluidic channels of GO film, and it was evidenced by the scanning electron microscope energy-dispersive system (SEM-EDS) shown in Figures S12A–S12F. Inductively coupled plasma-mass spectrometry (ICP-MS) was used to verify the increase in Li^+ in the GO film after discharge, with the content of lithium elements increasing from 863 ppm to 29,634 ppm (Figure 3A). In addition, the flame color experiment was carried out, and there was a characteristic carmine flame of the Li element in the discharged GO under a butane flame, while only a yellow flame from carbon was observed in the pristine GO (Figure 3B; Video S1). On the other hand, a slight increase in the average interlayer distance from 8.03 Å to 8.68 Å of the GO after discharge was observed (Figure 3C), which may be caused by the Li^+ diffusion within the nanofluidic channels. In addition, the increased relative intensity of defects in the Raman spectra (Figure 3D) may be also caused by the Li^+ intercalation. The disorder-induced band (D peak) is located near 1,350 cm^{-1}, and the graphite band (G peak) is close to 1,580 cm^{-1}. Before discharge, the intensity ratio (I_D/I_G) of GO was 1.005, which was lower than that of rGO at 1.115, suggesting that rGO itself had more structural defects, consistent with the previous SEM observations (Figure S7C). After discharge, the I_D/I_G ratio of GO increased to 1.054, suggesting the possible insertion of Li^+ inside the layers of GO but without major structural changes. In contrast, the I_D/I_G ratio of rGO decreased to 1.022, which may indicate a decrease in defects, possibly due to the removal of Li^+. The diffusion of Li^+ from rGO to GO was supported by the above characteristics, and the redox reactions at the ionic-electronic interface could also be designed. The optical microscope recorded some changes caused by redox reactions, as shown in Figure 3E. The pristine interface between GO and the Ag electrode contained a large amount of white transparent powders of $AgNO_3$ salts, while after the discharge, the silver-white Ag metallic particles were precipitated at the interface with a large amount of white opaque powder produced on the surface of GO that was verified as $LiNO_3$ by XRD (Figure S13). *In situ* FTIR, shown in Figure 3F, recorded the whole process. The peak at 800 cm^{-1} was considered the $v_2(A_2)$ vibrational mode of NO_3^- in pure $AgNO_3$,[45] corresponding to the contact ion pair with the Ag^+ cation. However, it moved to 829 cm^{-1} after discharge and showed a clear intensity transition state when the discharge time lasted up to 5 h. This may be due to the fact that the diffused Li^+ made the NO_3^- polarized to enhance the NO_3^- vibrational frequency and lead it to a higher wave number. Moreover, XPS observed a strong peak at 55.7 eV in the Li fine spectrum in the discharged GO, which is thought to be a Li-N bond[46] (Figure 3G). In addition, the transition state from $AgNO_3$ to $LiNO_3$ could be calculated by energetics along reaction coordination from density functional theory (DFT) (Figures 3H and S14A–S14C), and the energy of the whole process was reduced to −325.96 kJ mol^{-1}, which illustrated the replacement process of Ag^+ by Li^+. On the rGO side, optical microscopy showed the precipitation of a large number of white crystals at the interface, which was verified by XRD and EDS as

CellPress OPEN ACCESS

Cell Reports Physical Science Article

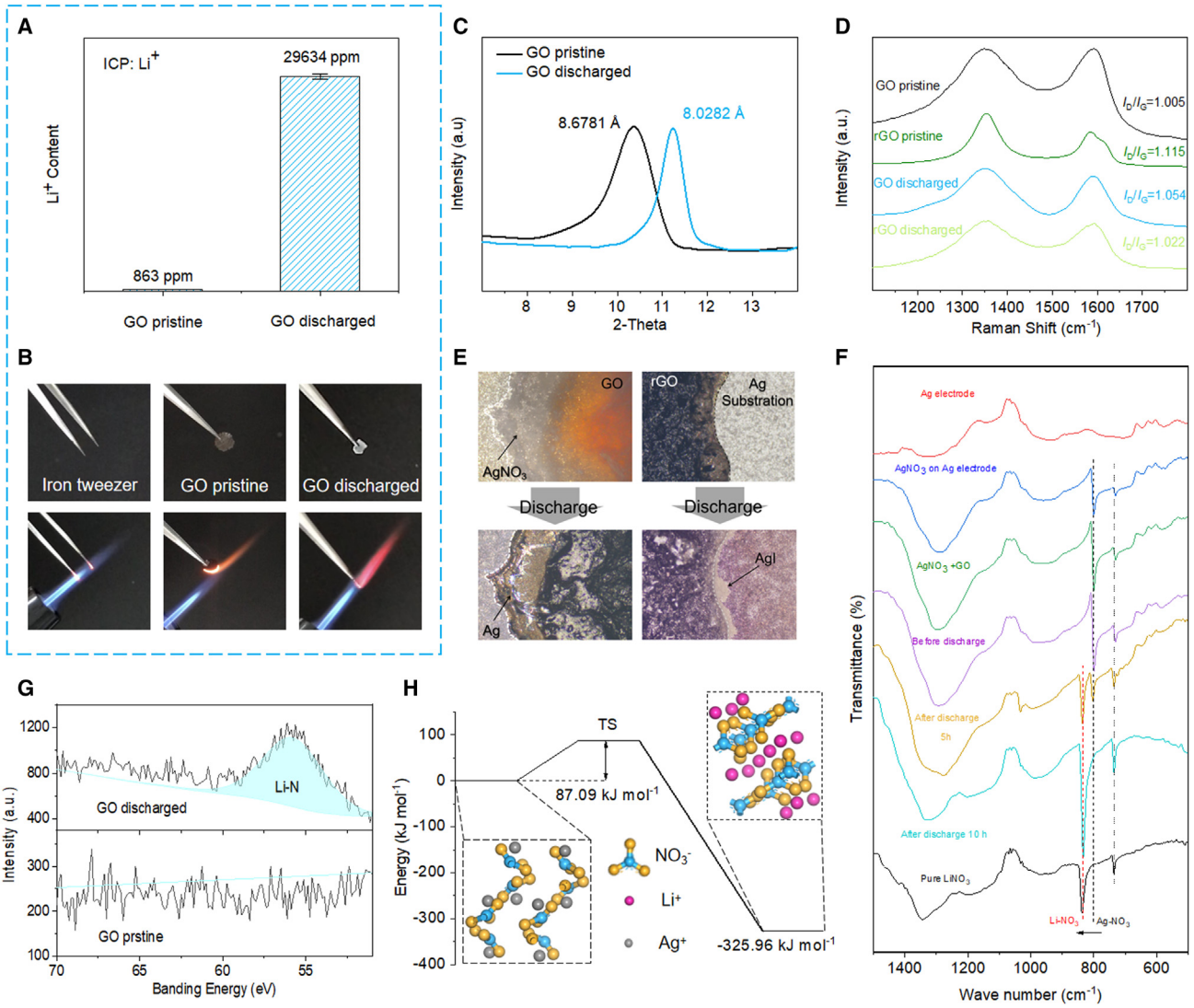

Figure 3. Redox reactions within GO nanoconfined channels

(A and B) Li^+ content (A) in the GO measured by ICP and the flame tests of the pristine and discharged GO (B) indicate Li^+ intercalation into GO during discharge.

(C) XRD characteristics of the pristine and discharged GO suggested an interlayer spacing change.

(D) Raman spectra of GO and rGO before and after discharge.

(E) Optical photographs of the Ag/$AgNO_3$-GO/LiI-rGO/Ag. Photographs were taken before (top) and after discharge (bottom).

(F) *In situ* FTIR characteristics for Ag/$AgNO_3$-GO/LiI-rGO/Ag; the peaks of the Ag electrode, pure $AgNO_3$, and $LiNO_3$ and the mixture of GO and $AgNO_3$ are shown as comparisons.

(G) XPS of GO before and after discharge.

(H) DFT-calculated energetics along reaction coordination.

the AgI (Figures S15 and S16). Faraday redox reactions at both sides were consistent with the theoretical calculations from the Nernst equation and provided a chemical built-in electric field in the solid-state iontronic power source, further facilitating the Li^+ diffusion within the GO.

Interfacial ion dynamics

Interfacial ion dynamics could provide a better insight into the coupling of ion diffusion and redox reactions. Figure 4A shows the CV curves of the iontronic

Please cite this article in press as: Peng et al., High-power iontronics enabled by nanoconfined ion dynamics, Cell Reports Physical Science (2024), https://doi.org/10.1016/j.xcrp.2024.101824

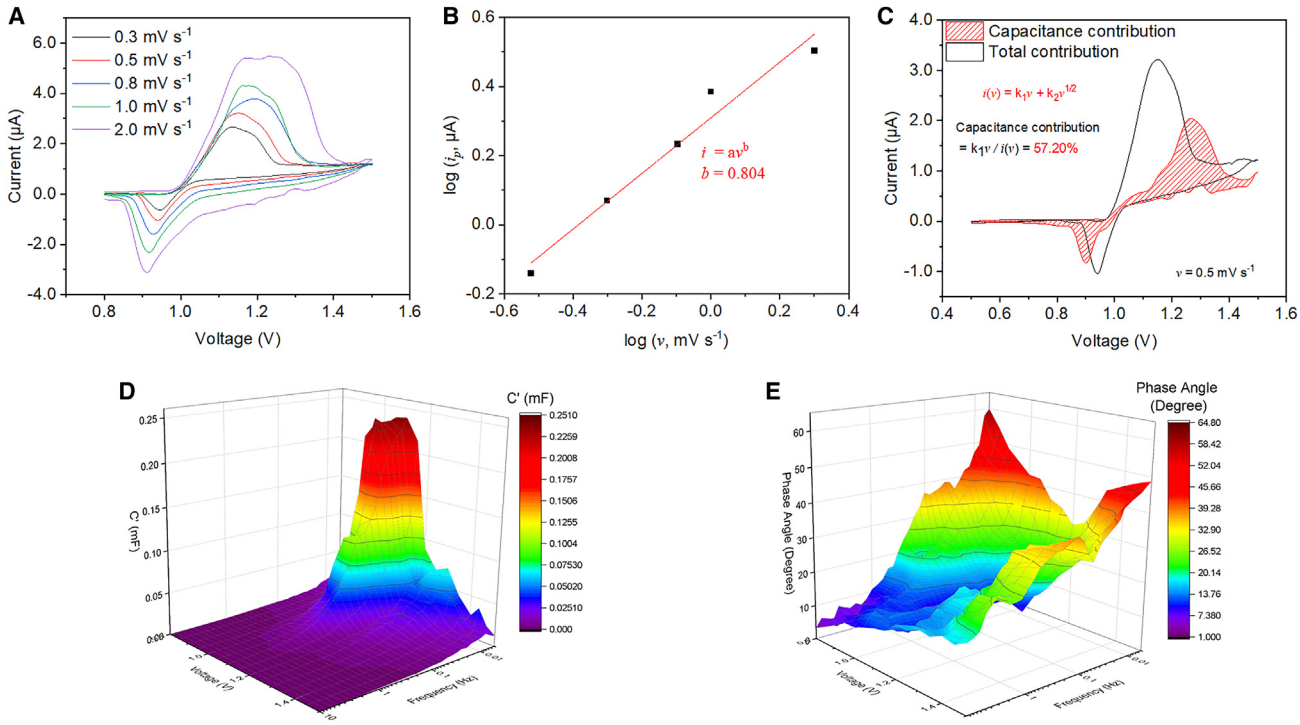

Figure 4. Interfacial ion dynamics

(A) CV test at different voltage scan rates from 0.8 mV s^{-1} to 1.5 mV s^{-1}.

(B) Corresponding log(i_p) versus log(v); the calculated *b* value is 0.804.

(C) Estimation of diffusion capacitance by pseudocapacitance method at 0.5 mV s^{-1}; the contribution of the capacitance is 57.20%.

(D and E) 3D Bode plot representations of the (D) real capacitance and (E) phase angle vs. frequency and voltage.

Ag/$AgNO_3$-GO/LiI-rGO/Ag in the voltage window from 0.8 to 1.5 V at scan rates from 0.3 mV s^{-1} to 2 mV s^{-1}. Each curve showed two broad redox peaks almost symmetrically superimposed on a rectangle-like profile, with a cathodic reduction region located at ~0.9 V and an anodic oxidation region at ~1.2 V. Thus, it is also rechargeable and can be stabilized for more than 100 cycles with a Coulombic efficiency of about 85%, as shown in Figures S17A and S17B. In addition, the voltammetric response of an electrode-active material at various scan rates can be summarized as the following equation:[47]

$$i_{(v)} = av^b \quad \text{(Equation 1)}$$

where *a* is a constant and *b* is the index that can be obtained from the slope of the plot of log(*i*) versus log(*v*). When *b* = 0.5, the rate-limiting step is indicated as a semi-infinite diffusion control of the Faraday reaction, and *b* = 1.0 suggests a surface limitation of the EDL. When the *b* value is in the range between 0.5 and 1.0, it is indicated as a finite diffusion process;[35,48] i.e., a pseudocapacitance process. As shown in Figure 4A, the peak currents $i_{(p)}$ obtained from the test were 0.73 μA, 1.17 μA, 1.71 μA, 2.42 μA, and 3.18 μA at the scan rates of 0.3, 0.5, 0.8, 1, and 2 mV s^{-1}, respectively. By analyzing the log(*i*) vs. log(*v*), as shown in Figure 4B, the *b* value was calculated to be about 0.804, which indicated that, within such a scan rate range, the interfacial ion dynamics were dominated by a high-rate, surface-controlled mechanism.[48] The voltammetric response could also be expressed as a combination of two independent contributions:[49]

$$i(v) = k_1 v + k_2 v^{1/2} \quad \text{(Equation 2)}$$

Please cite this article in press as: Peng et al., High-power iontronics enabled by nanoconfined ion dynamics, Cell Reports Physical Science (2024), https://doi.org/10.1016/j.xcrp.2024.101824

where k_1 and k_2 are the constants describing the surface control from EDL and diffusion control from redox, respectively. It could further provide the proportional contribution of the current generated by each process, which may help to estimate the contribution from the E_{diff}. As shown in Figure 4C, the obtained maximum percentage of the E_{diff} contribution is 57.20% for the iontronic power source with LiI, which is larger than 48.93% of the iontronic power source with LiCl (Figures S18A–S18C). The E_{diff} contribution was previously predicted as 45.83% in the liquid osmotic system (Note S2), further demonstrating that the introduced redox reaction generated a built-in electric field that could promote the iontronic energy.

In addition, the 3D Bode analysis from electrochemical impedance spectroscopy (EIS) could also be used to distinguish the capacitive, pseudocapacitive, or battery-like process.[35] It could be derived from a series of 2D plots, as shown in Figures S19A–S19C. The 3D Bode plot of Ag/$AgNO_3$-GO/LiI-rGO/Ag (Figure 4D) showed as a waterfall plot, as if the real capacitance (C′) bulged near the $E_{1/2}$ in the low-frequency region (<1 Hz) and revealed the pronounced redox responses. At other potentials, it exhibited capacitive-type responses, which was evident from the shape of the 3D map, as it is highly consistent with the corresponding CV data (Figure 4A). The phase angle (φ) probing shown in Figure 4E showed a wild deep slot from 1.1–1.25 V, where the redox behavior was prominent. The ionic-electronic interface exhibited potential-dependent φ behavior at low frequencies, signifying combination of capacitive and redox characteristics in the chosen potential window. Thus, the high power iontronics enabled by nanoconfined ion dynamics and interfacial redox reactions included both a fast capacitive process and a reversible Faraday redox process.

Fractal printable iontronics with device integration

Both power and energy of the iontronic power source could be boosted by the enhanced ion dynamics through the introduction of interfacial redox reactions coupled with the fast-diffusing Li^+ within the 2D nanofluidic channels. Such an iontronic power source was fully printable with the rheological optimized GO and rGO inks (Figure S20). Applying printing as the scale-up method in our case has a distinct advantage in designing fractal printable geometry that could maximize the length of the printed electrodes while occupying the smallest area to further enhance its power/energy density.[50] Such mathematical concepts of space-filling curves have been applied in designing various capacitors,[51] sensors, and antenna devices.[52]. The iontronic power source made by the GO and rGO inks also had a V_{oc} of 0.954 V and I_{sc} of 0.73 mA with a power/energy density of 1,566.25 mW cm^{-2}/119.28 mWh cm^{-2}, respectively, which were very close to those with the pristine GO/rGO junction (Figure S21). Thus, the additives had little influence on the performance of the device. The osmotic power source with the modified inks could be further printed in a large area by the ultrasonic extrusion printer (Video S2), making it scalable and providing the possibility of direct integration of circuit boards in a more versatile way.[24,25,53] Figures 5A and 5B also show a schematic of the fractal printing process of the osmotic power source with the print pattern of Peano curves.

As the length of the printing pattern is crucial for the output performance of the power source, the influence of it was studied in detail from 1 cm to 20 cm. The device with a length of 1 cm had an I_{sc} of less than 1 mA (Figure S22), in agreement with the above studies (Figure 2E). With the length of the printed circuit going up to 20 cm, the I_{sc} increased to 14 mA, exhibiting great prospects for real-world application. As a result, the ultrathin and printable osmotic power source could be integrated into different electronics. It could be simply cut with scissors without affecting the output voltage, as shown in Figure 5C and Video S3. Two cut cells in series (with total area of 0.12 cm^2) can make a

Please cite this article in press as: Peng et al., High-power iontronics enabled by nanoconfined ion dynamics, Cell Reports Physical Science (2024), https://doi.org/10.1016/j.xcrp.2024.101824

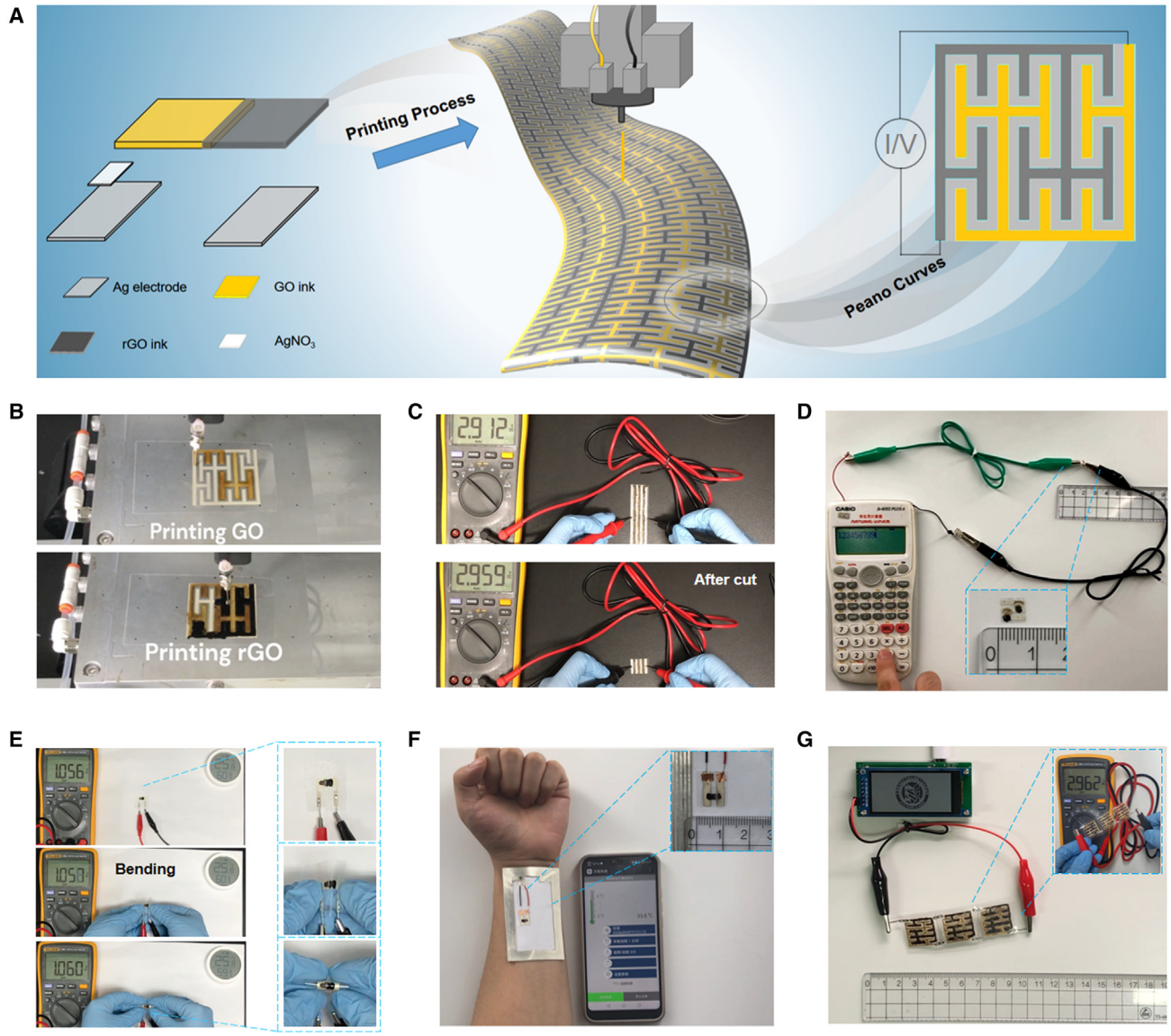

Figure 5. Fractal-printable iontronics and device integration

(A) Schematic of the printing process with the print pattern of Peano curves.
(B) Pictures of the printing process with the print pattern of Peano curves.
(C) Cutting test of the iontronic power source.
(D) Powering a calculator with the iontronic power source.
(E) Bending test of the iontronic power source.
(F) Driving conformable sensors for monitoring the temperature of the human body.
(G) Lighting up an LCD by three fractal-printed devices connecting in series.

calculator work (Figure 5D; Video S4). The flexibility of the device was further tested through either bending by hand (Figure 5E; Video S5) or further fatigue cycling over 1,000 times (bending radius of ~1 cm; Figure S23A). It showed no decay of performance under such severe bending conditions, and the I-V characteristics showed an I_{sc} of 0.68 mA and power density of 1489.82 mW cm^{-2} (Figure S23B) after being bent, which was similar to the pristine device. Such a conformable power source (with a total area of 0.4 cm^2) could replace a commercial battery in conformable sensors for monitoring temperature in the environment or human body (Figure 5F; Video S6). To power a more

Please cite this article in press as: Peng et al., High-power iontronics enabled by nanoconfined ion dynamics, Cell Reports Physical Science (2024), https://doi.org/10.1016/j.xcrp.2024.101824

energy-consuming device, longer electrodes are needed. As the fractal geometry enables maximum length in a given area, this concept was used to generate more current in our printable power source (Figure S24). Because the Peano curve has a larger fill length in a finite area compared with other space-filling curves, it was chosen as the printing pattern of our osmotic power source.[50] The cumulative device length can be up to ~17.5 cm in a finite area of 1.85 cm × 1.8 cm. This device was tested by I-V characteristics, showing an I_{sc} of ~12 mA (25°C, 80% RH; Figures S25A and S25B), similar to the results from previous studies (~14 mA in Figure S22) with similar length (20 cm). The power source scaled up with a print pattern of Peano curves (~17.5 cm) in a finite area could increase the power density up to 1,482.31 mW cm^{-2}, and the slight decrease in power density may stem from increased ionic resistance. However, three fractal-printed devices in series with a V_{oc} up to 2.962 V could also light up a liquid crystal display (LCD) even under ambient humidity (Figure 5G; Video S7). The fractal-printable iontronic power source could be easily integrated with a TENG (Figures S26, S27; Note S8) to form triboiontronic power management systems. Such self-powered triboiontronics could provide stable energy for futuristic wearable and implantable devices in neuron-computer interfaces, where ultrathin and safe energy sources are needed.

In summary, the charge attraction and steric effects in the nanoconfined space could restrict the disordered motion of ions, thus achieving anomalous ion dynamics. Here, the coupling of the fine-tuned interfacial Ag/Ag^+ redox reactions with the highly efficient unipolar transport of Li^+ within the 2D nanofluidic channels of GO was reported to enable solid-state high power iontronics. It could achieve an areal energy density of ~1.4 kWh m^{-2} and power density of ~16.07 kW m^{-2}, which is beyond most Li^+ batteries and supercapacitors, respectively. The efficient transport of Li^+ within GO nanofluidic channels was illustrated by ICP-MS, the flame color experiment, and Raman spectroscopy. For $AgNO_3$ dispersed in the nanoconfined GO channels, Ag^+ would be replaced by Li^+ and the process was recorded by *in situ* FTIR, where the transition peaks of NO^{3-} in FTIR moved to high wave number under polarization by the diffused Li^+. In addition, the Li-N bond was observed by XPS, while both the formation of $LiNO_3$ and Ag metal were evidenced by XRD and optical microscopy. DFT calculations also supported the observed transition state from $AgNO_3$ to $LiNO_3$. Reversible Ag/Ag^+ redox reactions at both sides were designed that could be determined by the Nernst equation and provided a chemical built-in electric field in this solid-state iontronic power source, further facilitating the Li^+ diffusion within the GO. The reaction kinetics were verified by dynamic calculations via CV and 3D Bode analysis, which showed that the interfacial ion dynamics were dominated by a high-rate, surface-controlled mechanism. Such an iontronic power source could also be printed in a scalable or fractal way and overcome self-discharge when kept under extremely low humidity conditions and be cut safely with scissors to meet the energy needs of a variety of electronic devices. In addition, integrated with the energy-harvesting TENG, it could form conformable and self-charging triboiontronics. This work could also be the first attempt to bring such ultrathin (~10.5 μm) and portable iontronic power source into practical applications to provide stable energy support for self-driven health monitoring, wearable electronics, and even future implementations in human-machine or neuronal-computer interfaces. In nature, chemiosmotic coupling was used to explain the redox conversion of adenosine diphosphate (ADP) to ATP through the effective proton transport driven by the ion gradient, as shown in Figure S28.[54] We analogously propose a paradigm for the synergy of effective ion transport within nano-hierarchical structures and interfacial redox reactions, and it could be further expanded to understand the coupling interface between electronic and ionic signals for wider prospective applications.

Please cite this article in press as: Peng et al., High-power iontronics enabled by nanoconfined ion dynamics, Cell Reports Physical Science (2024), https://doi.org/10.1016/j.xcrp.2024.101824

EXPERIMENTAL PROCEDURES

Resource availability

Lead contact

Further information and requests for resources and reagents should be directed to and will be fulfilled by the lead contact, Di Wei (weidi@binn.cas.cn).

Materials availability

The materials in this study are available from the lead contact upon reasonable request.

Data and code availability

The data generated in this study are available from the lead contact upon reasonable request.

Materials

GO was prepared from graphite powders (XFNANO) using a modified Hummers' method. Graphite powders (1 g), H_3PO_4 (2 mL), and H_2SO_4 (21 mL) were premixed in an ice water bath, and afterward $KMnO_4$ (3 g) was slowly added to react for 2 h. Then the solution was transferred to a 35°C water bath and stirred for ~0.5 h to form a thick paste. After that, 46 mL of deionized (DI) water was slowly added, and the paste with water was transferred to a 95°C water bath for 15 min. Finally, 140 mL of water and 10 mL of H_2O_2 (30%) were added. After washing away soluble salts and incompletely reacted graphite by centrifuge, the GO powder could be finally obtained from the GO dispersion by freeze drying. The GO solution (5 mg mL^{-1}) was prepared by dissolving 50 mg GO powder with 10 mL DI water. rGO was prepared by mixing 0.2 g GO and 0.2 g LAA in a round-bottom flask with 195 mL H_2O and hydrochloric acid (37%, 5 mL) and stirred vigorously at 60°C for 5 h. All related chemicals (H_2SO_4, $KMnO_4$, H_2O_2, H_3PO_4, and LAA) and the hydrochloric acid (37%) etc. were purchased from Sigma-Aldrich and were used as received. DI water with a resistivity of above 18 MΩ cm^{-1} was collected from a Mili-Q Biocel system.

Fabrication of the flexible Ag charge collector

The commercial PET film was thoroughly cleaned with abundant acetone, alcohol, and DI water with a bath sonicator. A computer-controlled commercial CO_2 laser cutter system was used to cut the PET film into A4 size. Afterward, screen-printable Ag ink, purchased from Changsung, was printed on PET by using the predesigned screen-printing patterns. The obtained substrates were dried in an oven at 130°C for 30 min. GO and the rGO solutions were deposited onto the PET substrate with screen-printed Ag strips as charge collectors.

Preparation of printing inks

GO ink

Nafion perfluorinated resin solution (5 wt %) was purchased from Sigma-Aldrich, and the GO ink was prepared by simply mixing 8 mL of GO aqueous dispersion (5 mg mL^{-1}) and 2 mL of Nafion solution (5 wt %).

rGO ink

Sodium dodecyl sulfate (SDS) was purchased from Sigma-Aldrich, and the rGO ink was prepared by ultrasonicating mixed 50 mg rGO and 4 mg SDS in 10 mL DI water in 30 min.

All inks were uniformly dispersed with ultrasonication for 30 min before printing.

Characterization and measurements

The morphologies of the devices were observed by the SEM (SU8020, Hitachi) with the 5.0-kV accelerating voltage and 10 μA emission current, and EDS was used for the element analysis. Dektak XT Stylus Profiler (Bruker) was used to profile the morphology of the planar osmotic power sources and provides information on volume values for the calculation of specific energy and power density. Raman spectra were collected with the LabRAM HR Evolution (Horiba) with a 532-nm laser. FTIR data were collected by Bruker VERTEX80v. For the TENG characterization, a step motor (LinMot E1100) was used to provide the input of mechanical motions. The voltage and current output were recorded by a Keithley electrometer 6514. Zeta potentials were obtained by using a Beckman Coulter instrument (Delsamax Pro). Particle size analysis was performed with BLUEWAVE S3500 (Microtrac) with a 408-nm laser.

Electrochemical measurements and humidity control

The electrochemical measurements, unless otherwise stated, were carried out in the Voetsch 4018C environmental chamber to control temperature and RH. All electrochemical measurements were carried out with the electrochemical workstation (Multi Autolab M204).

Bending fatigue tests

A custom-made mechanical bend testing system with a three-point bending fixture was used to analyze the planar osmotic power source under a fatigue cycling test. Typically, a 4 × 2-cm sample was loaded on two bars, with an actuator pressing onto the sample with a specific deformation in the z direction (downwards). In our measurements, a span length of 2 cm was fixed for the sample, and the deformation was 2 cm from the flat position, providing a bending radius of ~1 cm per cycle. The bending system was set up inside an environmental chamber, allowing us to perform tests on the power source under various environmental conditions. The fatigue tests of 1,000 mechanical cycles were carried out at a frequency of 1 Hz under 80% RH and 25°C. The I-V characteristics of the power source showed unaffected performance after the fatigue tests.

DFT calculations

All calculations based on DFT were carried out in the Dmol3 module of Materials Studio 2020. The generalized gradient approximation (GGA) and PW91 density functional method (GGA-PW91) were used to calculate the exchange correlation energy. The binding energy (ΔE) between two components was obtained as follows:

$$\Delta E = E(A^+ - NO_3^-) - E(A^+) - E(NO_3^-)$$

where $E(A^+ - NO_3^-)$, $E(A^+)$ and $E(NO_3^-)$ are the total energies of the $A^+ - NO_3^-$ complexes, A^+ cation, and NO_3^- anion, respectively.

In the calculation, linear synchronous transit (LST) and quadratic synchronous transit (QST) tools were used to search for transition states. Considering the calculation efficiency and calculation accuracy comprehensively, the system accuracy was set to medium accuracy, and the track thermal occupation adopted the default 0.01 Hartree. By calculating the reaction energy, the reaction path with the lowest activation energy was the most likely reaction path.

SUPPLEMENTAL INFORMATION

Supplemental information can be found online at https://doi.org/10.1016/j.xcrp.2024.101824.

ACKNOWLEDGMENTS

This work was supported by the Beijing Natural Science Foundation (grant IS23040). Volunteers took part in the experiments involving wearables following informed consent.

AUTHOR CONTRIBUTIONS

D.W. and Z.W. proposed the idea and supervised the whole project. D.W. and P.P. designed all experiments and wrote this paper. P.P. conducted the experiments and DFT calculations. F.Y. designed and screen-printed the Ag electrodes and carried out the bending tests. X.L. and S.L. performed the fabrication and tests of TENG and analyzed its data. All authors discussed the results and commented on the manuscript.

DECLARATION OF INTERESTS

The authors declare no competing interests.

Received: November 20, 2023
Revised: January 3, 2024
Accepted: January 18, 2024
Published: February 8, 2024

REFERENCES

1. Shen, J., Liu, G., Han, Y., and Jin, W. (2021). Artificial channels for confined mass transport at the sub-nanometre scale. Nat. Rev. Mater. *6*, 294–312. https://doi.org/10.1038/s41578-020-00268-7.

2. Qian, H., Wei, D., and Wang, Z. (2023). Bionic iontronics based on nano-confined structures. Nano Res. *16*, 11718–11730. https://doi.org/10.1007/s12274-023-5705-z.

3. Zhong, J., Alibakhshi, M.A., Xie, Q., Riordon, J., Xu, Y., Duan, C., and Sinton, D. (2020). Exploring Anomalous Fluid Behavior at the Nanoscale: Direct Visualization and Quantification via Nanofluidic Devices. Acc. Chem. Res. *53*, 347–357. https://doi.org/10.1021/acs.accounts.9b00411.

4. Forse, A., Griffin, J., Merlet, C., Carretero-Gonzalez, J., Raji, A.R., Trease, N., and Grey, C. (2017). Direct observation of ion dynamics in supercapacitor electrodes using in situ diffusion NMR spectroscopy. Nat. Energy *2*, 16216. https://doi.org/10.1038/nenergy.2016.216.

5. Chen, L., Shi, G., Shen, J., Peng, B., Zhang, B., Wang, Y., Bian, F., Wang, J., Li, D., Qian, Z., et al. (2017). Ion sieving in graphene oxide membranes via cationic control of interlayer spacing. Nature *550*, 380–383. https://doi.org/10.1038/nature24044.

6. Xue, Y., Xia, Y., Yang, S., Alsaid, Y., Fong, K.Y., Wang, Y., and Zhang, X. (2021). Atomic-scale ion transistor with ultrahigh diffusivity. Science (New York, N.Y.) *372*, 501–503. https://doi.org/10.1126/science.abb5144.

7. Wang, M., Hou, Y., Yu, L., and Hou, X. (2020). Anomalies of Ionic/Molecular Transport in Nano and Sub-Nano Confinement. Nano Lett. *20*, 6937–6946. https://doi.org/10.1021/acs.nanolett.0c02999.

8. Daiguji, H. (2010). Ion transport in nanofluidic channels. Chem. Soc. Rev. *39*, 901–911. https://doi.org/10.1039/b820556f.

9. Zhan, H., Xiong, Z., Cheng, C., Liang, Q., Liu, J.Z., and Li, D. (2020). Solvation-Involved Nanoionics: New Opportunities from 2D Nanomaterial Laminar Membranes. Adv. Mater. *32*, e1904562. https://doi.org/10.1002/adma.201904562.

10. Feng, J., Liu, K., Graf, M., Dumcenco, D., Kis, A., Di Ventra, M., and Radenovic, A. (2016). Observation of ionic Coulomb blockade in nanopores. Nat. Mater. *15*, 850–855. https://doi.org/10.1038/nmat4607.

11. Yang, Q., Sun, P.Z., Fumagalli, L., Stebunov, Y.V., Haigh, S.J., Zhou, Z.W., Grigorieva, I.V., Wang, F.C., and Geim, A.K. (2020). Capillary condensation under atomic-scale confinement. Nature *588*, 250–253. https://doi.org/10.1038/s41586-020-2978-1.

12. Li, Z., Misra, R.P., Li, Y., Yao, Y.-C., Zhao, S., Zhang, Y., Chen, Y., Blankschtein, D., and Noy, A. (2023). Breakdown of the Nernst-Einstein relation in carbon nanotube porins. Nat. Nanotechnol. *18*, 177–183. https://doi.org/10.1038/s41565-022-01276-0.

13. Wen, L., Zhang, X., Tian, Y., and Jiang, L. (2018). Quantum-confined superfluid: From nature to artificial. Sci. China Mater. *61*, 1027–1032. https://doi.org/10.1007/s40843-018-9289-2.

14. van de Burgt, Y., Lubberman, E., Fuller, E.J., Keene, S.T., Faria, G.C., Agarwal, S., Marinella, M.J., Alec Talin, A., and Salleo, A. (2017). A non-volatile organic electrochemical device as a low-voltage artificial synapse for neuromorphic computing. Nat. Mater. *16*, 414–418. https://doi.org/10.1038/nmat4856.

15. Yue, Z. (2021). Ionic gating for ion intercalation. Nat. Rev. Phys. *3*, 306. https://doi.org/10.1038/s42254-021-00311-8.

16. Chen, K., Hu, H., Song, I., Gobeze, H.B., Lee, W.-J., Abtahi, A., Schanze, K.S., and Mei, J. (2023). Organic optoelectronic synapse based on photon-modulated electrochemical doping. Nat. Photonics *17*, 629–637. https://doi.org/10.1038/s41566-023-01232-x.

17. Xing, Y., Zhou, M., Si, Y., Yang, C.-Y., Feng, L.-W., Wu, Q., Wang, F., Wang, X., Huang, W., Cheng, Y., et al. (2023). Integrated opposite charge grafting induced ionic-junction fiber. Nat. Commun. *14*, 2355. https://doi.org/10.1038/s41467-023-37884-0.

18. Weintrub, B.I., Hsieh, Y.-L., Kovalchuk, S., Kirchhof, J.N., Greben, K., and Bolotin, K.I. (2022). Generating intense electric fields in 2D materials by dual ionic gating. Nat. Commun. *13*, 6601. https://doi.org/10.1038/s41467-022-34158-z.

19. Ye, T., Hou, G., Li, W., Wang, C., Yi, K., Liu, N., Liu, J., Huang, S., and Gao, J. (2021). Artificial sodium-selective ionic device based on

crown-ether crystals with subnanometer pores. Nat. Commun. *12*, 5231. https://doi.org/10.1038/s41467-021-25597-1.

20. Boahen, E.K., Pan, B., Kweon, H., Kim, J.S., Choi, H., Kong, Z., Kim, D.J., Zhu, J., Ying, W.B., Lee, K.J., and Kim, D.H. (2022). Ultrafast, autonomous self-healable iontronic skin exhibiting piezo-ionic dynamics. Nat. Commun. *13*, 7699. https://doi.org/10.1038/s41467-022-35434-8.

21. Yang, R., Dutta, A., Li, B., Tiwari, N., Zhang, W., Niu, Z., Gao, Y., Erdely, D., Xin, X., Li, T., and Cheng, H. (2023). Iontronic pressure sensor with high sensitivity over ultra-broad linear range enabled by laser-induced gradient micro-pyramids. Nat. Commun. *14*, 2907. https://doi.org/10.1038/s41467-023-38274-2.

22. Feng, J., Graf, M., Liu, K., Ovchinnikov, D., Dumcenco, D., Heiranian, M., Nandigana, V., Aluru, N.R., Kis, A., and Radenovic, A. (2016). Single-layer MoS2 nanopores as nanopower generators. Nature *536*, 197–200. https://doi.org/10.1038/nature18593.

23. Kim, S., Choi, S., Lee, H.G., Jin, D., Kim, G., Kim, T., Lee, J.S., and Shim, W. (2021). Neuromorphic van der Waals crystals for substantial energy generation. Nat. Commun. *12*, 47. https://doi.org/10.1038/s41467-020-20296-9.

24. Wei, D., Yang, F., Jiang, Z., and Wang, Z. (2022). Flexible iontronics based on 2D nanofluidic material. Nat. Commun. *13*, 4965. https://doi.org/10.1038/s41467-022-32699-x.

25. Yang, L., Yang, F., Liu, X., Li, K., Zhou, Y., Wang, Y., Yu, T., Zhong, M., Xu, X., Zhang, L., et al. (2021). A moisture-enabled fully printable power source inspired by electric eels. Proc. Natl. Acad. Sci. USA *118*, e2023164118. https://doi.org/10.1073/pnas.2023164118.

26. Chouhdry, H.H., Lee, D.H., Bag, A., and Lee, N.-E. (2023). A flexible artificial chemosensory neuronal synapse based on chemoreceptive ionogel-gated electrochemical transistor. Nat. Commun. *14*, 821. https://doi.org/10.1038/s41467-023-36480-6.

27. Stein, D., Kruithof, M., and Dekker, C. (2004). Surface-charge-governed ion transport in nanofluidic channels. Phys. Rev. Lett. *93*, 035901. https://doi.org/10.1103/PhysRevLett.93.035901.

28. Cui, G., Xu, Z., Li, H., Zhang, S., Xu, L., Siria, A., and Ma, M. (2023). Enhanced osmotic transport in individual double-walled carbon nanotube. Nat. Commun. *14*, 2295. https://doi.org/10.1038/s41467-023-37970-3.

29. Zhang, Z., Yang, S., Zhang, P., Zhang, J., Chen, G., and Feng, X. (2019). Mechanically strong MXene/Kevlar nanofiber composite membranes as high-performance nanofluidic osmotic power generators. Nat. Commun. *10*, 2920. https://doi.org/10.1038/s41467-019-10885-8.

30. Lu, P., Xia, Y., Sun, G., Wu, D., Wu, S., Yan, W., Zhu, X., Lu, J., Niu, Q., Shi, S., et al. (2023). Realizing long-cycling all-solid-state Li-In|| TiS(2) batteries using Li(6+x)M(x)As(1-x)S(5)I (M=Si, Sn) sulfide solid electrolytes. Nat. Commun. *14*, 4077. https://doi.org/10.1038/s41467-023-39686-w.

31. Zhao, X., Liu, M., Wang, Y., Xiong, Y., Yang, P., Qin, J., Xiong, X., and Lei, Y. (2022). Designing a Built-In Electric Field for Efficient Energy Electrocatalysis. ACS Nano *16*, 19959–19979. https://doi.org/10.1021/acsnano.2c09888.

32. Veerman, J., Saakes, M., Metz, S.J., and Harmsen, G.J. (2010). Reverse electrodialysis: evaluation of suitable electrode systems. J. Appl. Electrochem. *40*, 1461–1474. https://doi.org/10.1007/s10800-010-0124-8.

33. Huang, Y., Cheng, H., Yang, C., Yao, H., Li, C., and Qu, L. (2019). All-region-applicable, continuous power supply of graphene oxide composite. Energy Environ. Sci. *12*, 1848–1856. https://doi.org/10.1039/c9ee00838a.

34. Liu, X., Gao, H., Ward, J.E., Liu, X., Yin, B., Fu, T., Chen, J., Lovley, D.R., and Yao, J. (2020). Power generation from ambient humidity using protein nanowires. Nature *578*, 550–554. https://doi.org/10.1038/s41586-020-2010-9.

35. Choi, C., Ashby, D.S., Butts, D.M., DeBlock, R.H., Wei, Q., Lau, J., and Dunn, B. (2019). Achieving high energy density and high power density with pseudocapacitive materials. Nat. Rev. Mater. *5*, 5–19. https://doi.org/10.1038/s41578-019-0142-z.

36. Cao, L., Guo, W., Ma, W., Wang, L., Xia, F., Wang, S., Wang, Y., Jiang, L., and Zhu, D. (2011). Towards understanding the nanofluidic reverse electrodialysis system: well matched charge selectivity and ionic composition. Energy Environ. Sci. *4*, 2259. https://doi.org/10.1039/c1ee01088c.

37. Guo, W., Cao, L., Xia, J., Nie, F.-Q., Ma, W., Xue, J., Song, Y., Zhu, D., Wang, Y., and Jiang, L. (2010). Energy Harvesting with Single-Ion-Selective Nanopores: A Concentration-Gradient-Driven Nanofluidic Power Source. Adv. Funct. Mater. *20*, 1339–1344. https://doi.org/10.1002/adfm.200902312.

38. Raidongia, K., and Huang, J. (2012). Nanofluidic ion transport through reconstructed layered materials. J. Am. Chem. Soc. *134*, 16528–16531. https://doi.org/10.1021/ja308167f.

39. Zhang, Z., Wen, L., and Jiang, L. (2021). Nanofluidics for osmotic energy conversion. Nat. Rev. Mater. *6*, 622–639. https://doi.org/10.1038/s41578-021-00300-4.

40. Li, C., Wen, L., Sui, X., Cheng, Y., Gao, L., and Jiang, L. (2021). Large-scale, robust mushroom-shaped nanochannel array membrane for ultrahigh osmotic energy conversion. Sci. Adv. *7*, eabg2183. https://doi.org/10.1126/sciadv.abg2183.

41. Kopec, W., Köpfer, D.A., Vickery, O.N., Bondarenko, A.S., Jansen, T.L.C., de Groot, B.L., and Zachariae, U. (2018). Direct knock-on of desolvated ions governs strict ion selectivity in K(+) channels. Nat. Chem. *10*, 813–820. https://doi.org/10.1038/s41557-018-0105-9.

42. Pu, Q., Yun, J., Temkin, H., and Liu, S. (2004). Ion-Enrichment and Ion-Depletion Effect of Nanochannel Structures. Nano Lett. *4*, 1099–1103. https://doi.org/10.1021/nl0494811.

43. Kim, S.J., Wang, Y.-C., Lee, J.H., Jang, H., and Han, J. (2007). Concentration polarization and nonlinear electrokinetic flow near a nanofluidic channel. Phys. Rev. Lett. *99*, 044501. https://doi.org/10.1103/PhysRevLett.99.044501.

44. Ando, K., Liu, A.-Q., and Ohl, C.-D. (2012). Homogeneous nucleation in water in microfluidic channels. Phys. Rev. Lett. *109*, 044501. https://doi.org/10.1103/PhysRevLett.109.044501.

45. Meng, N., Ma, X., Wang, C., Wang, Y., Yang, R., Shao, J., Huang, Y., Xu, Y., Zhang, B., and Yu, Y. (2022). Oxide-Derived Core-Shell Cu@Zn Nanowires for Urea Electrosynthesis from Carbon Dioxide and Nitrate in Water. ACS Nano *16*, 9095–9104. https://doi.org/10.1021/acsnano.2c01177.

46. Wang, J., Zhang, J., Duan, S., Li, T., Jia, L., Liu, H., Li, L., Cheng, S., Hu, H., Huang, M., et al. (2022). Interfacial lithium-nitrogen bond catalyzes sulfide oxidation reactions in high-loading Li2S cathode. Chem. Eng. J. *429*, 132352. https://doi.org/10.1016/j.cej.2021.132352.

47. Lindström, H., Södergren, S., Solbrand, A., Rensmo, H., Hjelm, J., Hagfeldt, A., and Lindquist, S.-E. (1997). Li+ Ion Insertion in TiO2 (Anatase). 2. Voltammetry on Nanoporous Films. J. Phys. Chem. B *101*, 7717–7722. https://doi.org/10.1021/jp970490q.

48. Wu, P., Wu, J., Si, H., Zhang, Z., Liao, Q., Wang, X., Dai, F., Ammarah, K., Kang, Z., and Zhang, Y. (2020). 3D Holey-Graphene Architecture Expedites Ion Transport Kinetics to Push the OER Performance. Adv. Energy Mater. *10*. https://doi.org/10.1002/aenm.202001005.

49. Wang, J., Polleux, J., Lim, J., and Dunn, B. (2007). Pseudocapacitive Contributions to Electrochemical Energy Storage in TiO2 (Anatase) Nanoparticles. J. Phys. Chem. C *111*, 14925–14931. https://doi.org/10.1021/jp074464w.

50. Moselhy, T., Ragaie, H.F., and Haddara, H. (2003). Investigation of space filling capacitors. In Proceedings of the 12th IEEE International Conference on Fuzzy Systems (Cat. No.03CH37442, pp. 287–290. https://doi.org/10.1109/ICM.2003.237831.

51. Thekkekara, L.V., Chen, X., and Gu, M. (2018). Two-photon-induced stretchable graphene supercapacitors. Sci. Rep. *8*, 11722. https://doi.org/10.1038/s41598-018-30194-2.

52. Fan, J.A., Yeo, W.H., Su, Y., Hattori, Y., Lee, W., Jung, S.Y., Zhang, Y., Liu, Z., Cheng, H., Falgout, L., et al. (2014). Fractal design concepts for stretchable electronics. Nat. Commun. *5*, 3266. https://doi.org/10.1038/ncomms4266.

53. Ali, M.A., Hu, C., Yuan, B., Jahan, S., Saleh, M.S., Guo, Z., Gellman, A.J., and Panat, R. (2021). Breaking the barrier to biomolecule limit-of-detection via 3D printed multi-length-scale graphene-coated electrodes. Nat. Commun. *12*, 7077. https://doi.org/10.1038/s41467-021-27361-x.

54. Mitchell, P. (1961). Coupling of phosphorylation to electron and hydrogen transfer by a chemi-osmotic type of mechanism. Nature *191*, 144–148. https://doi.org/10.1038/191144a0.

Cell Reports Physical Science, Volume *5*

Supplemental information

High-power iontronics enabled by nanoconfined ion dynamics

Puguang Peng, Feiyao Yang, Xiang Li, Shaoxin Li, Zhonglin Wang, and Di Wei

Table of contents

Note S1| The real ionic diffusion area

The ions are rapidly transported through the horizontal GO nanoconfined channels, where the dimensional data of GO are shown in Figure S1E-G with a length of *l*: 4.98 mm, a width of *w*: 2.01 mm and a height of *h*: ~5 μm. Also, the height of the channel can be characterized by XRD as shown in Figure S2A-B. First, in the infiltrated type-confined GO, the layer spacing can still remain at *d*: 8.8539 Å, and the thickness of GO is about *t*: 3.4 Å. Therefore, the height of the channel can be predicted to be $D = d - t = 5.55$ Å, from which the cross-sectional area of the ion diffusion in GO is inferred to be

$$\mathrm{A} = l \times h \times \frac{d - t}{d} = 1.56 \times 10^{-8}\ m^2$$

In addition, in all-solid iontronics, the 3D profile is shown in Figure S9A-B, and similarly, the cross-sectional area of its ion diffusion can be estimated as

$$\mathrm{A}' = l' \times h' \times \frac{d' - t}{d'} = 1.05 \times 10^{-8}\ m^2$$

where the l' is 3.7 mm, h' is 5.5 μm and the d' is 8.03 Å.

Note S2| Thermodynamics in osmotic systems: both the ionic diffusion and the Faraday redox are essential.

The process of chemical gradient to electrical energy conversion can be well understood by using thermodynamic diffusion theory [1].

Under isothermal and equal pressure, two liquids with ionic salinity gradients (C_H and C_L) are mixed and the total amount of ions passing at their liquid interface in a very short time (dt) is dn mol, then the flux of cations is $t_+ dn$ mol and the flux of anions is $t_- dn$ mol, and there is

$$dn = t_+ dn + t_- dn \quad (\text{Also } t_+ + t_- = 1) \tag{S1}$$

According to the definition of chemical potential:

$$\mu_i = \mu_0 + RT \ln \alpha_i$$

where μ is the chemical potential, μ_0 is the standard chemical potential, and R, T, and α are the universal gas constant, temperature and the activity of matters, respectively.

Taking the direction of cation diffusion as the positive direction, the chemical potential difference between cation and anion can be expressed respectively as

$$\Delta\mu_+ = (\mu_{+,0} + RT \ln a_{+,\mathrm{L}}) - (\mu_{+,0} + RT \ln a_{+,\mathrm{H}}) = RT \ln \frac{a_{+,\mathrm{L}}}{a_{+,\mathrm{H}}}$$

$$\Delta\mu_- = (\mu_{-,0} + RT \ln a_{-,\mathrm{L}}) - (\mu_{-,0} + RT \ln a_{-,\mathrm{H}}) = RT \ln \frac{a_{-,\mathrm{L}}}{a_{-,\mathrm{H}}}$$

Thus, according to the thermodynamic equation below:

$$dG = -SdT + Vdp + \sum \mu_i dn_i$$

At isothermal isobaric pressure, the Gibbs free energy energies of cations and anions could become:

$$dG_+ = RT \ln \frac{a_{+,\mathrm{L}}}{a_{+,\mathrm{H}}} dn_+ = RT \ln \frac{a_{+,\mathrm{L}}}{a_{+,\mathrm{H}}} t_+ dn$$

$$dG_- = RT \ln \frac{a_{-,\mathrm{L}}}{a_{-,\mathrm{H}}} dn_- = RT \ln \frac{a_{-,\mathrm{L}}}{a_{-,\mathrm{H}}} t_- dn$$

When there are no ion selective channels, the total change in the Gibbs free energy of the system can be expressed as

$$dG = dG_+ + dG_- = RT \ln \frac{a_{+,\mathrm{L}}}{a_{+,\mathrm{H}}} t_+ dn + RT \ln \frac{a_{-,\mathrm{L}}}{a_{-,\mathrm{H}}} t_- dn \tag{S2}$$

meanwhile, in this liquid system, Li^+ and Cl^- have the same valence state and the concentration change of the bulk ions can be neglected before the ions have migrated at the moment of mixing,

so it can be assumed that

$$\frac{a_{+,\mathrm{L}}}{a_{+,\mathrm{H}}} = \frac{a_{-,\mathrm{L}}}{a_{-,\mathrm{H}}}$$

and according to the definition of activity, $a_{\pm}^2 = a_+ a_-$ there is

$$\frac{a_{\mathrm{L}}}{a_{\mathrm{H}}} = \frac{a_{+,\mathrm{L}}}{a_{+,H}} = \frac{a_{-,L}}{a_{-,H}} \tag{S3}$$

and also by Faraday's law, the relationship with the $dn_{\pm}$ and ionic current ($|I_{\pm}|$) can be predicted as follows:

$$dQ_{\pm} = F dn_{\pm} = |I_{\pm}| dt$$

$$dn_{\pm} = \frac{dt}{F}|I_{\pm}| \tag{S4}$$

uniting the equation (S1-4) yields:

$$\begin{aligned} dG &= -(t_+ + t_-)RT\ln\frac{\alpha_H}{\alpha_L}dn = -\frac{RT}{F}\ln\frac{\alpha_H}{\alpha_L}|I_0|dt \\ &= -\frac{RT}{F}\ln\frac{\alpha_H}{\alpha_L}(|I_+| + |I_-|)dt \end{aligned} \tag{Equation 1}$$

Here, I_+ and I_- are the diffusion current contributed by Li^+ or Cl^-. Equation 1 shows the total change in Gibbs free energy during the migration of positive and negative ions in the same direction.

However, under the selection of the nanoconfined channels, the cations and anions diffusing rates would be different and inducing the net Gibbs energy change (dG_{net}) in the system. In this system, GO acts as a cation channel and the net Gibbs free energy change can be expressed as

$$dG_{net} = dG_{+} - dG_{-} = RT\ln\frac{a_{+,L}}{a_{+,H}}t_{+}dn - RT\ln\frac{a_{-,L}}{a_{-,H}}t_{-}dn$$
$$= -(t_{+} - t_{-})RT\ln\frac{a_H}{a_L}dn \quad \text{(S5)}$$

The Gibbs energy change at isothermal and isobaric pressure can be transformed into reversible non-volume work, so the electric work caused by the net current (I_{net}) due to the selected ions diffusion can be defined as

$$dW = -dG_{net} = FEdn \quad \text{(S6)}$$

and there is

$$I_{net} = |I_{+}| - |I_{-}|, \quad t_{+} = \frac{|I_{+}|}{|I_{+}| + |I_{-}|} \quad \text{and} \quad t_{-} = \frac{|I_{-}|}{|I_{+}| + |I_{-}|} \quad \text{(S7)}$$

uniting the equation (S5-7) yields:

$$dW_{diff} = (t_{+} - t_{-})RT\ln\frac{a_H}{a_L}\frac{dt}{F}|I_{net}| = \frac{RT}{F}\frac{(|I_{+}| - |I_{-}|)^2}{|I_{+}| + |I_{-}|}\ln\frac{\alpha_H}{\alpha_L}dt \quad \text{(Equation 2)}$$

and $$E_{diff} = (t_{+} - t_{-})\frac{RT}{F}\ln\frac{a_H}{a_L} \quad \text{(Equation 3)}$$

where E_{diff} is the diffusion potential, which is generated by the net diffusion of cations and anions.

After the numerical transformation, the Equation 2 can be changed to

$$dW_{diff} = \frac{RT}{F}\ln\frac{a_H}{a_L}\left[\left(\frac{|I_{+}| - |I_{-}|}{|I_{+}| + |I_{-}|}\right)^2(|I_{+}| + |I_{-}|)\right]dt$$

$$dW_{diff} = \frac{RT}{F}\ln\frac{a_H}{a_L}(t_{+} - t_{-})^2|I_0|dt$$

$$dW_{diff} = (t_{+} - t_{-})\frac{RT}{F}\ln\frac{a_H}{a_L}(t_{+} - t_{-})|I_0|dt = E_{diff}(t_{+} - t_{-})|I_0|dt \quad \text{(Equation 4)}$$

The above Equation 4 can be interpreted as, that the value of dW_{diff} can be estimated by using the area value enclosed by the I-t curve, which can be obtained from Chronoamperometry

(CA) test under the applied bias slightly below the E_{diff}. This is because and the value of t_+ and t_- could be kept constant when the concentration gradient is still. However, note that the conversion of ionic currents into electronic currents is usually carried out by redox couples during this test, and a standard Ag/AgCl electrode is required to avoid reaction interference. Thus, the dW_{diff} caused by pure ionic diffusion $\ln(C_H / C_L) = 3$ is obtained as approximately 189.1 μWh as shown in Figure S3A.

On the other hand, Ag electrodes are used in this system to form redox couples with Cl^- in solution, and the reactions of Ag exposed in different Cl^- concentrations can be expressed as

$$Ag_{(s)} + Cl^-_{(aq,\,H)} \rightarrow AgCl_{(s)} + e^-$$

$$AgCl_{(s)} + e^- \rightarrow Ag_{(s)} + Cl^-_{(aq,\,L)}$$

From the Nernst equation, it can be inferred that the redox voltage (E_{redox}) is

$$E_{redox} = \frac{RT}{F} \ln \frac{a_{(Cl^-,\,H)}}{a_{(Cl^-,\,L)}} \qquad \text{(Equation 5)}$$

and the electrical work (dW_{redox}) generated by the redox pair can be expressed as

$$dW_{redox} = E_{redox}\, I_{redox}\, dt = \frac{RT}{F} \ln \frac{a_{(Cl^-,\,H)}}{a_{(Cl^-,\,L)}} I_{redox}\, dt \qquad \text{(Equation 6)}$$

Remarkably, Equation 1 and Equation 6 are very similar, but the diffusion current (I_0) and the redox current (I_{redox}) are caused by very different sources. In redox systems, the built-in electric field constructed by the chemical reaction will cause the cation to move toward the cathode and the anion to move toward the anode, so the net ionic current of the anion and cation is the I_{redox} . However, the current contributions of cation and anion diffusion will cancel each other out when ion-selective channels are not present in diffusion systems, which will make the dG cannot be converted to dW_{diff} .

The value of dW_{redox} can also be estimated by CA curve, as shown in Figure S3B, where the energy is 203.7 μWh obtained at the $\ln(C_H / C_L) = 3$.

Thus, when using Ag electrodes in diffusion systems with ion-selective channels that is possible to study the energy output contributed by redox and osmosis simultaneously, with the value tested of ~412.6 μWh as shown in Figure S3C. This value is greater than the sum of pure osmotic energy and redox energy, which may be due to the magnitude of the osmotic potential is highly related to the t_+ while the redox potential is more related to the anion gradient according to the Equation 3 and Equation 5 (the latter is from Nernst equation), and the ion-selective channels promote cation diffusion and create a barrier to anion diffusion.

Therefore, both the ionic diffusion and the Faraday redox are essential for this system, and a rough estimate of the percentage of osmotic energy is about 45.83% by using the results obtained from the above separate CA tests in liquid system.

Note S3| Ion diffusion kinetics

GO as a cation-selective channel will lead to the polarization of anions and cations centered on GO for separation, at which time the strength of the built-in electric field composed of the salinity gradients can be expressed as:

$$\vec{E} = \frac{xq}{4\pi\varepsilon\varepsilon_0 d^2}$$

where x, q, ε, ε_0 and d is the number of ions, basic charge constant, relative permittivity of water, vacuum permittivity and channel length, respectively. In our tests, the length of the GO channels is 2.01 mm and the diffusion voltage is ~0.162 V formed at $\ln(C_H / C_L) = 3$. Therefore, by the defining equation of the electric field it can be calculated that

$$\vec{E} = \frac{V}{d} = 53\ V\ m^{-1}$$

Combining the above equations yields that the number of cations is $1.78*10^7$ to be diffused to maintain a voltage of 0.162 V. This is significantly less than the number of cations in our added solution of 200uL of 1M LiCl ($1.2*10^{25}$).

Therefore, the steady-state diffusion can be considered at this instant, and the diffusion coefficient of cations in GO nanoconfined channels was calculated by using the results in Figure S4A-F combined with the following Fick's first law:

$$D = \frac{J \times L}{\Delta C}$$

where D, J, L and ΔC are the diffusion coefficient, ion flux, channel length and concentration, respectively.

The ion flux is defined as the ionic passing moles number through a unit area of the plane per unit time, and combined with Faraday's law, it is obtained that

$$J = \frac{n}{A} = \frac{I}{FA}$$

where I is the ion current, F is the Faraday constant, and A is the cross-sectional area of the ion channel.

Thus, the diffusion coefficients at different concentration gradients can be obtained, as shown in Figure 1G. It shows an increasing trend as the concentration gradient increases, which may be related to the enhancement of the ionic current in the system.

Note S4| The calculations of ion mobility

Due to the large negative charge on the GO surface, there is a strong selecting effect on

the cations in solution and a limited ionic current is observed even without applied voltage as shown in the I-V curve from Figure S4A-F, which becomes shifted along the voltage axis. Therefore, the ratio of the mobility of the cation to that of the anion can be calculated using the Henderson equation [2]:

$$\frac{\mu^+}{\mu^-} = -\frac{z_+ \ln(\Delta) - z_- F E_m / RT}{z_- \ln(\Delta) - z_+ F E_m / RT}$$

Here, z_+ and z_- are the valences of cations and anions, F is the Faraday constant, R is the universal gas constant, T is the absolute temperature, Δ is the concentration gradient, and E_m is the diffusion potential (E_{diff}).

In parallel, GO can also exhibit ultra-high ionic conductance at low concentrations under the electrostatic effect from surface charge (Figure S5A-C). However, the conductance at high concentrations is essentially the same as in bulk solution, so the effect can be neglected, and the conductivity at this point can be described as

$$G = F(\mu^+ + \mu^-)c\frac{wh}{l}$$

where c is the concentration of the LiCl solution, w, h and l are the width, height and length of the channels, respectively.

The mobilities of the cation under different gradients can be found by combining the above equations, as shown in Figure 1G. In addition, it is verified in general agreement with the diffusion coefficient calculated by Fick's law by the following Einstein's relation equation.

$$u = zeD / k_B T$$

where z is the valence of ions, e is the basic charge constant, D is the diffusion coefficient, and K_b is the Boltzmann constant.

Note S5| Non-homogeneous nucleation of water in nanoconfined channels

The additional pressure exerted on the liquid varies with the surface curvature, so the state of the liquid with unequal surface curvatures are different. This relationship can be described by the Kelvin equation [3]:

$$\frac{P_v}{P_{sat}} = exp(-\frac{2\gamma_l V_l}{r^* RT})$$

where P_v is the equilibrium vapor pressure, P_{sat} is the saturation vapor pressure, for aqueous the value of $\frac{P_v}{P_{sat}}$ can be considered as the relative humidity (RH), γ_l is the surface tension of the liquid (0.0721 N m^{-1} for water, 298 K), and V_l is the molar volume of the liquid ($V_l = \frac{Mr}{\rho}$, Mr is the molar mass, ρ is the density). r^* is the average curvature radius of the liquid bending surface, which can be considered as the radius of a small liquid droplet in vapor, R is the gas constant, and T is the temperature.

GO has a large number of hydrophilic functional groups and thus exhibits negative electricity, so that water can well infiltrate GO with a contact angle of 28.65° as shown in Figure S6A-B. The nanoconfined gaps formed between single GO layers is similar to capillaries, and we assume that capillary condensation (non-homogeneous condensation) occurs preferentially in such nano-gaps when exposed to the vapor atmosphere of water. Therefore, in the GO channel, the relationship between the channel aperture size (D) and the radius of curvature (r^*) can be expressed as

$$D = d - t = r^* cos\theta = -\frac{2\gamma_l V_l}{RTln\frac{P_v}{P_{sat}}} cos\theta$$

where d is the layer spacing obtained from XRD, t is the thickness of the monolayer GO

and D is 0.447 nm according to Note S1, θ is the contact angle between GO and water.

With the above equations, there is

$$\frac{P_v}{P_{sat}} = \exp(-\frac{2\gamma_l V_l}{DRT} cos\theta)$$

and taking the data into account, the $\frac{P_v}{P_{sat}}$ could be calculated as 0.13138. Thus, at a relative humidity greater than 13.14%, capillary condensation would occur in the GO channels, which is in general agreement with the results obtained from our experiments as shown in Figure 2F, where the current increasing gradually may be caused by the GO channels slowly opens and allows the ionic diffusion.

Note S6| All-solid ionic gradients predicted by the Nernst equation

The energy of the planar iontronics with high osmotic power is mainly based on adjustable redox reactions at the interface. The Nernst equation is used to calculate the voltage introduced by the redox reaction. However, since our device is operating as a solid-state power source, the Nernst equation could be used to only estimate the potential, as shown below.

$$Ag^+ + e^- \rightleftharpoons Ag \qquad E_c^0 = 0.80\ V$$

$$Ag + X^- \rightleftharpoons AgX + e^- \qquad E_a^0 = 0.22\ V, 0.07\ V\ and\ -0.15\ V\ (for\ X = Cl,\ Br\ and\ I)$$

Thus, the E_{redox} for iontronics with different lithium halides from LiCl, LiBr and LiI are 0.58 V, 0.73V and 0.95 V, respectively.

In fact, the V_{oc} of the measured iontronic power source is always slightly higher than the theoretically calculated value, as shown in Figure 2B. This is because the measured V_{oc} actually consists of two components, including the cation diffusion part (E_{diff}) and the redox part (E_{redox}) as discussed in Note S2.

$$V_{oc} = E_{diff} + E_{redox}$$

Therefore, the E_{diff} could be obtained from the following equation:

$$E_{diff} = V_{oc} - E_{redox}$$

according to the Equation 3, the ion concentration gradients can be estimated as about 10^6 – 10^7, thus having the ability to generate high power and high energy.

Note S7| Power and energy density of the all-solid iontronic power source

In Figure 2F, the generated power as calculated from the applied voltage and the measured current in Figure 2E —is plotted against the voltage generated in the iontronics. Therefore, according to the definition of the power generation, the max areal power generation from the iontronics is simply given as:

$$P_{max,\,aera} = \frac{I_{max} V_{max}}{A}$$

where I_{max}, V_{max} is the highest current and the corresponding voltage obtained in Figure 2E. A is the cross-sectional area for GO channels as discussed in Note S1.

Similarly, the max aera iontronic energy ($dW_{max,\,aera}$) can be calculated by

$$dW_{max,\,aera} = \frac{IVdt}{A}$$

where *I*, *V*, *t* is the iontronic current and the tested potential during discharge time, respectively, which could be calculated in Figure 2G.

Therefore, according to Figure 2F, the $P_{max,\,aera}$ of the iontronics could be calculated as 1607.14 mW cm^{-2}, 661.74 mW cm^{-2} and 245.64 mW cm^{-2} for iontronics loaded with LiI, LiBr and LiCl in rGO respectively, and the corresponding $dW_{max,\,aera}$ for those devices is 139.16 mWh cm^{-2}, 70.83 mWh cm^{-2}, 49.36 mWh cm^{-2}, respectively.

Note S8| Conformable Self-charging Triboiontronics

The neuron-computer interfaces currently could only be powered by energy harvesting devices with power in the range from μW to mW[4], which requires a self-charging unit to provide continuous energy. Our ultra-thin and conformable iontronic power source as an energy storage unit can be well adapted to the human's movement, which is superior to the conventional batteries/supercapacitors with rigid structure. Integrated with triboelectric nanogenerator (TENG) to form triboiontronics, it could be self-charged and provide much higher power and energy. The triboiontronics power management system could also mitigate the discontinuities input of TENG caused by intermittent motion and mismatched resistance [5, 6]. TENG could work by ubiquitous friction and does not rely on environmental factors such as sunlight, wind, humidity, etc. Compared to other energy harvesting devices, its fabrication is safer and more environmentally friendly without toxic electrolytes or complex manufacturing process. TENG has higher energy conversion efficiency than other methods in the frequency range of human motions. A flexible triboelectric nanogenerator (F-TENG) based on the copper-nickel-coated conductive cloth was designed, as the schematic structure shown in Figure S26A. Based on the coupling effect of contact electrification and electrostatic induction, the F-TENG could generate triboelectric potential and displacement current to charge the power source (as illustrated in Figure S26B). In F-TENG, two pieces of conductive fabric intersecting each other were used as electrode layers, and Kapton material was used as an independent friction layer. The structure design of this freestanding triboelectric-layer mode enables the electrode layer and friction layer independent of each other and could be posted on both sides of the underarm space. When walking or running, the F-TENG could harvest the frictional energy and generate

continuous electric energy output to charge the iontronic power source, extending its normal working time. The working principle of the F-TENG was shown in Figures S25C-F.

In terms of the output characteristics, the output of F-TENG at different frequencies of 1 Hz, 2 Hz, and 3 Hz was tested by using a linear motor as the driving unit. As shown in Figure S26A-B with the increase in frequency, the transferred charge (Q_{sc}) and V_{oc} output by the F-TENG remained around 41 nC and 100 V, respectively. However, when the frequency was increased from 1 Hz to 3 Hz, the I_{sc} output by the F-TENG increases from 0.15 μA to 0.5 μA (Figure S27C), which also lead to the faster charging at higher frequencies. As shown in Figure S20D, at the frequency of 3 Hz, the F-TENG with a bridge rectifier could charge a 22 μF capacitor to 1.5 V within 225s. The triboiontronic integration of F-TENG and iontronic power source could synergize the energy output (Figure S27E) by extended discharge time of the iontronic power source (Figure S27F). After the subsequent withdrawal of the F-TENG, the separated osmotic power can continue to discharge up to 20h. Such synergistic systems will greatly extend the lifetime of this disposable power source and may lead to potential applications for future low-power implantable devices.

Supplemental Figures

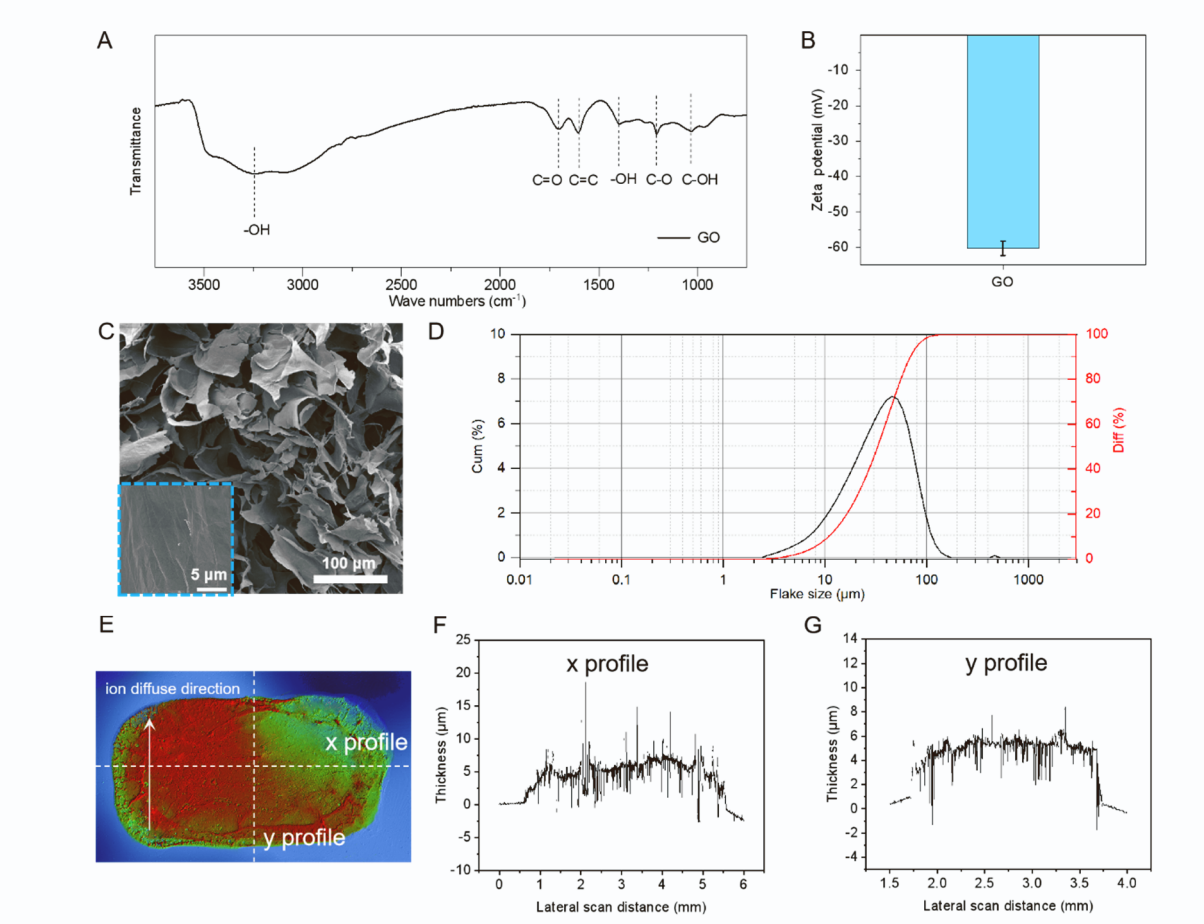

Figure S1. Characterization for GO. (A) Fourier transform infrared spectroscopy (FTIR) showing the characteristic peaks of functional groups on GO, where a broad peak at ~3300 cm^{-1} is the hydroxyl group (-OH), and the absorption bands at 1710, 1610, 1426, 1220 and 1020 cm^{-1} correspond to the stretching vibration of C=O in the carboxyl group, C=C on the sp_2 carbon skeleton, C-OH group on the carbonyl group (-COOH), C-O-C group and C-O group on the epoxy group, respectively. **(B)** Zeta potential test of GO dispersion showing a zeta potential of -60.28 mV. **(C)** SEM images of GO, showing the morphological features of the GO. **(D)** Laser particle size distribution test shows a major flake size of approximately 38 μm for GO. **(E-G)** Surface profile of the GO (E). The height of the GO is about 5 μm while the length (F) and width (G) is 4.98 mm and 2.01 mm, respectively.

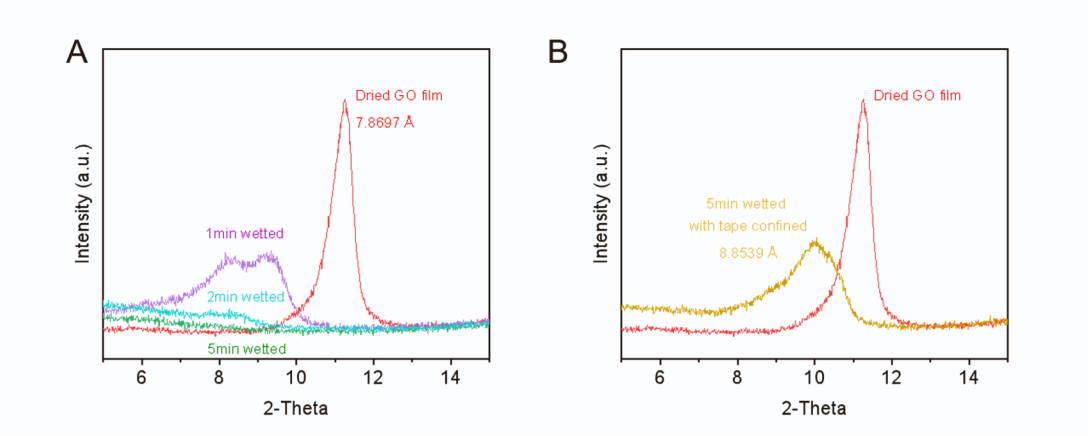

Figure S2. XRD patterns of GO film. (A) the dried GO and wetted GO by water. **(B)** acrylic tape-confined GO after wetted 5mins.

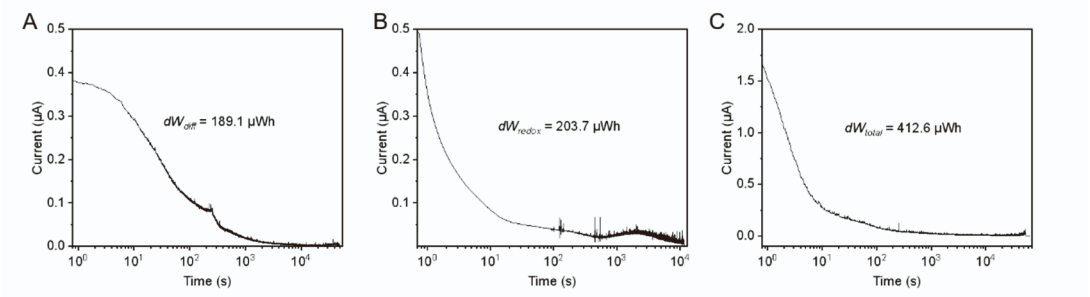

Figure S3. Chronoamperometry test to estimate the energy of ion diffusion, redox and total contribution in liquid system. (A) dW_{diff} = 189.1 μWh, **(B)** dW_{redox} = 203.7 μWh, **(C)** dW_{total} = 412.6 μWh.

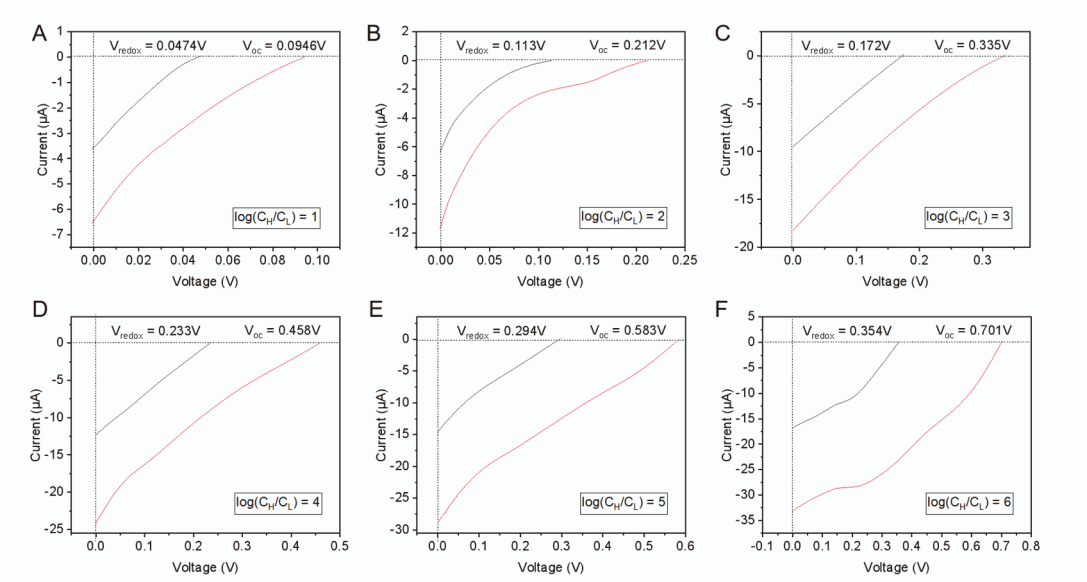

Figure S4. Voltage and current output of total and redox contribution with different gradients. (A-F) $\ln(C_H / C_L) = 1\sim6$.

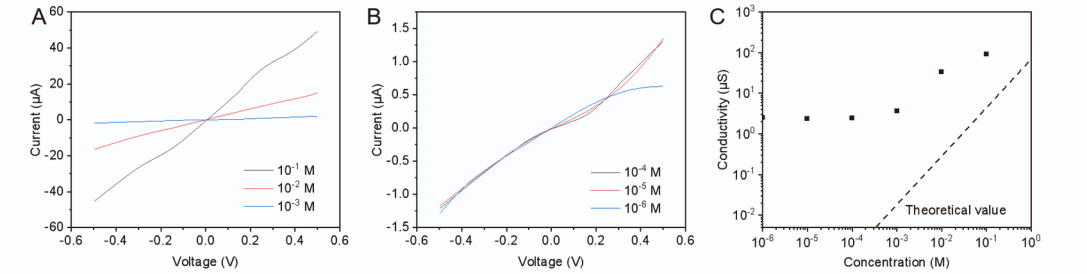

Figure S5. Conductance of the GO according to the different gradients. (A) I-V curves of GO from gradients of 10^{-1} - 10^{-3}. **(B)** I-V curves of GO from gradients of 10^{-4} – 10^{-6}**. (C)** Conductance plot.

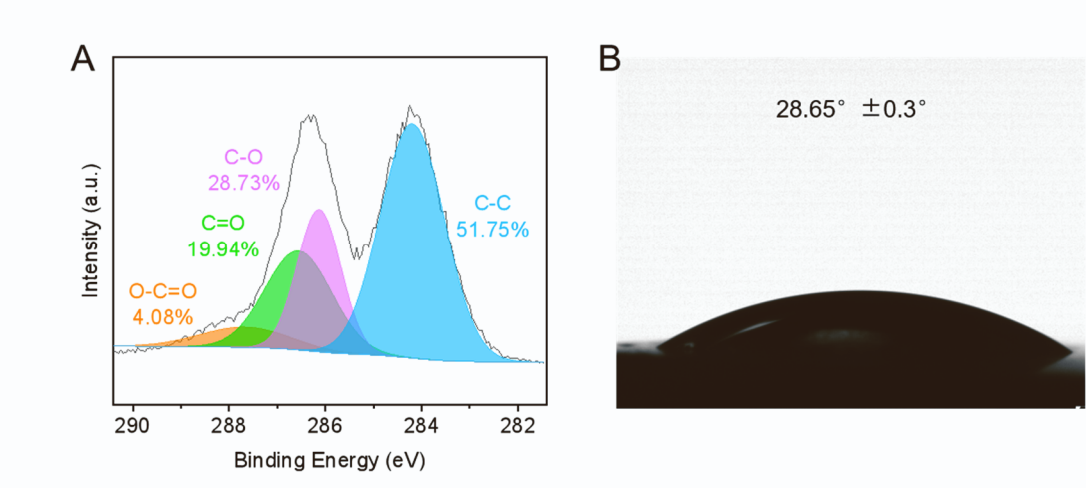

Figure S6. (A) X-ray photoelectron spectroscopy (XPS) spectra and **(B)** surface contact angle of water on GO. C 1s spectra were decomposed into four single peaks corresponding to four types of carbon bonds: C=C (284.4 eV, 51.75%), C–O (286.3 eV, 28.73%), C=O (286.7 eV, 19.94%), and O–C=O (219.8 eV, 4.08%).

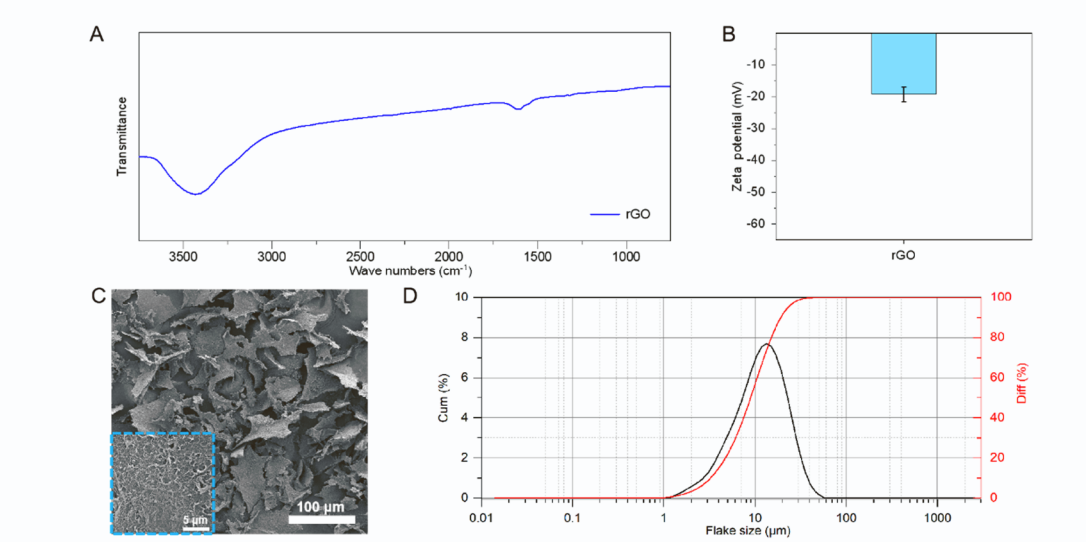

Figure S7. Characterization for rGO. (A) FTIR showing nearly no characteristic peaks of functional groups on rGO, where a broad peak at ~3300 cm^{-1} could be hydroxyl group (-OH). **(B)** Zeta potential test of GO dispersion showing a zeta potential of -18.04 mV. **(C)** SEM images of rGO, showing the porous structure. **(D)** Laser particle size distribution test shows a major flake size of approximately 15 μm for rGO.

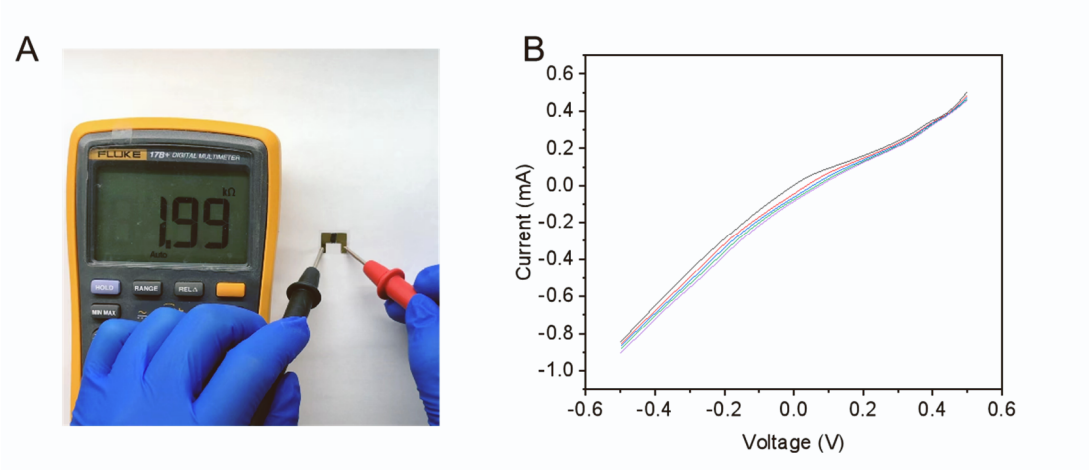

Figure S8. Characterization of the resistance of rGO. (A) Multimeter shows rGO resistance of 1.99 kΩ. **(B)** I-V test for rGO between Au electrodes.

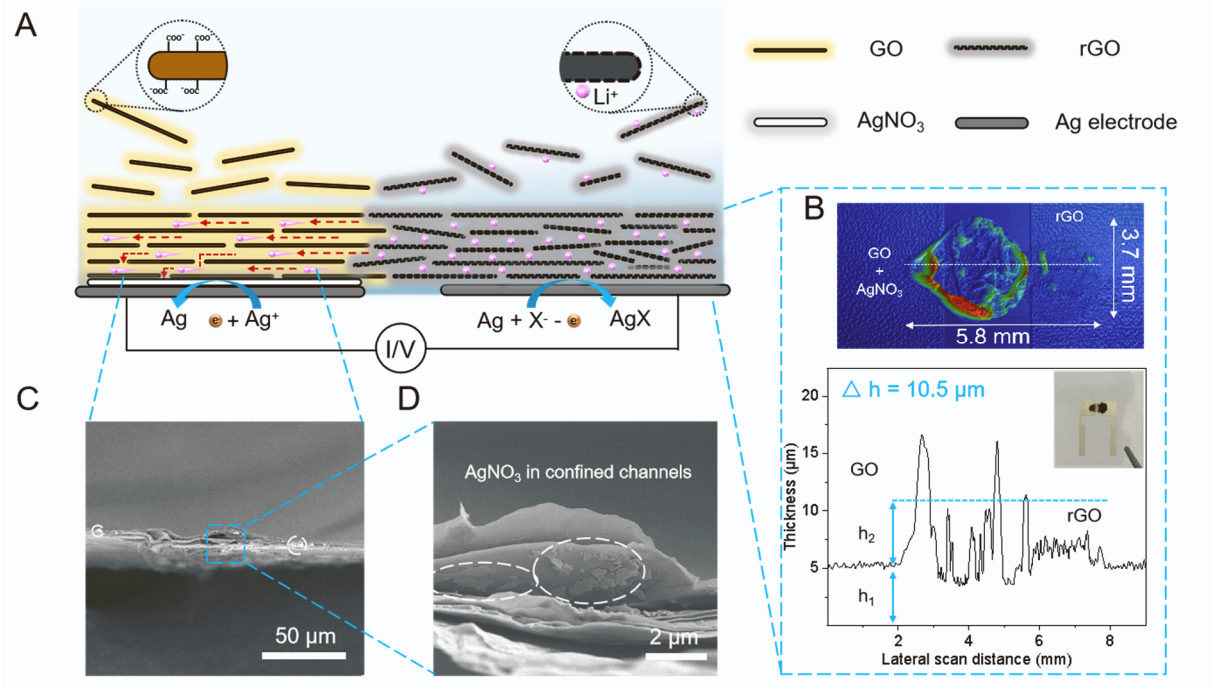

Figure S9. Characterization of the iontronic power source. (A) Layout structure of the iontronic power source. **(B)** Surface profile of the iontronic power source. The height of the charge collector (h_1) and the GO/rGO coating (h_2) is about 5 μm and 5.5 μm respectively. **(C-D)** SEM images of the (C) GO layer (cross-section) and the (D) $AgNO_3$ in confined channels.

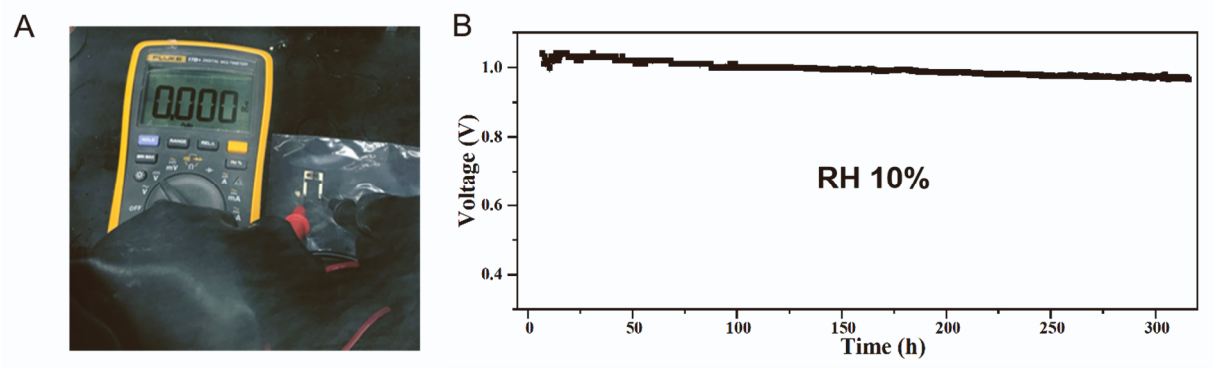

Figure S10. Low humidity to overcome the self-discharge. (A) There is no voltage under extremely low RH in the glovebox (H_2O < 10 ppm). **(B)** Open circuit voltage retention at RH = 10% over 300h.

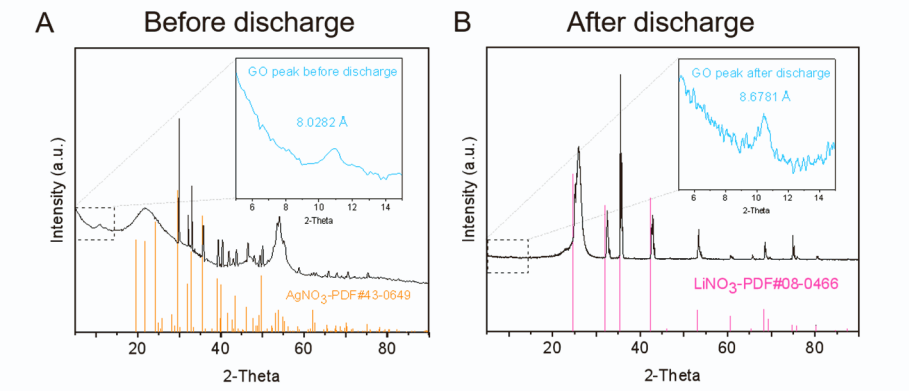

Figure S11. (A-B) The sample-to-sample variations of the I-V characteristics for the iontronic power source loaded with different salt in rGO. The mismatch of the curves may be caused by environmental humidity fluctuations

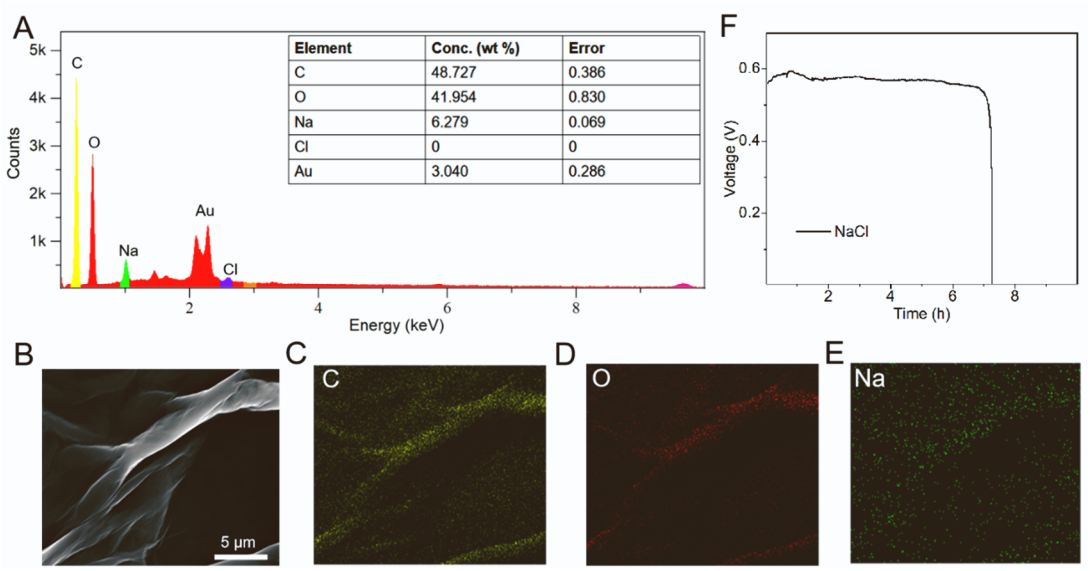

Figure S12. Characteristics of the Ag/$AgNO_3$-GO/NaCl-rGO/Ag iontronic power source. **(A)** EDX of the discharged Ag/$AgNO_3$-GO/NaCl-rGO/Ag, proving the transport of Na^+ through GO. **(B)** SEM image of the discharged GO in Ag/$AgNO_3$-GO/NaCl-rGO/Ag iontronic power source; **(C-E),** Corresponding EDX mapping images on the discharged GO for (C) C; (D) O; (E) Na. **(F)** The discharge curve of the Ag/$AgNO_3$-GO/NaCl-rGO/Ag iontronic power source, demonstrating the voltage of the iontronic power source is independent on the type of cations.

The elemental mapping shows the significant presence of cations and almost absence of anions in discharged GO. SEM-EDS could excite the atoms by X-rays and measure the secondary-ray energy to determine the type and relative content of elements. However, the ionization energy of Li atoms is very low, so that is easily ionized and quickly diffuse out of the analysis area, making them difficult to detect by EDS [7]. An alternative scheme uses Na^+ as the diffusion ions since iontronics using NaCl-rGO have similar electrochemical properties to LiCl-rGO as shown in Figure S12f. However, its energy density was lower due to the higher ionic resistance faced by the larger ionic radius of Na^+.

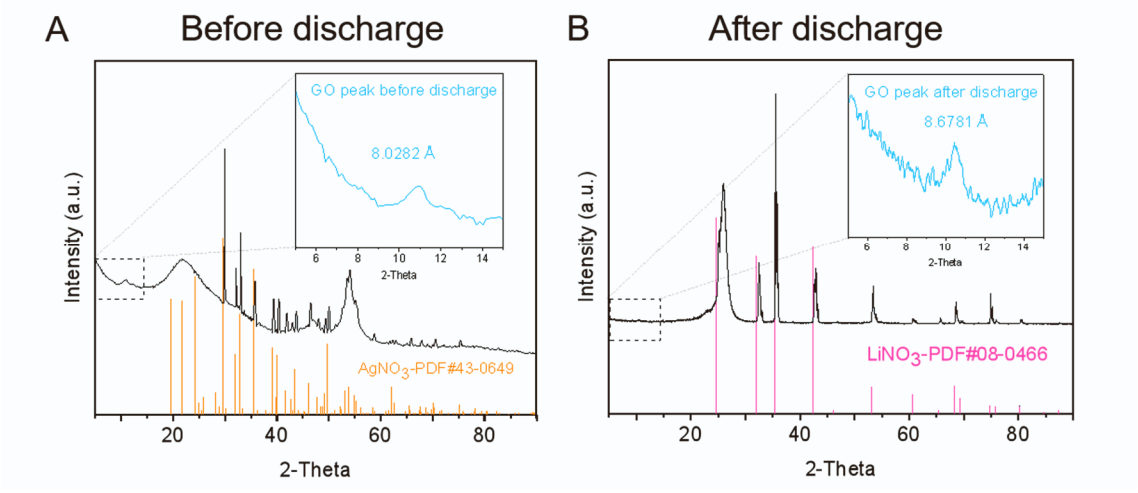

Figure S13. Characteristics of the GO side after discharge. (A-B) The XRD pattern obtained from the GO side before (A) and after discharge (B), showing the formation of $LiNO_3$, and it is noteworthy that both the $AgNO_3$ and $LiNO_3$ lattices are shifted to a high angle overall, which may be due to the potential resistance effect of the nanoconfined channels, as the layer spacing of pristine GO is larger than dried GO as shown in Figure S2.

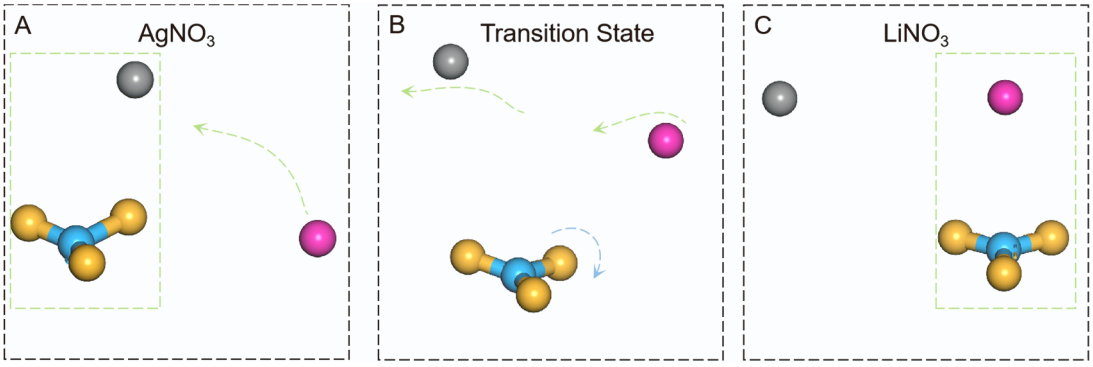

Figure S14. The process of the state along reaction coordination by DFT calculation. (A) Single-molecule $AgNO_3$ with tetrahedral structure and a Li^+ at pristine. **(B)** the transition sate of the reaction showing the continues process of Li^+ replace the Ag^+ and the structure changed. **(C)** Single-molecule $LiNO_3$ with triangular conical structure and an Ag^+ after replacement.

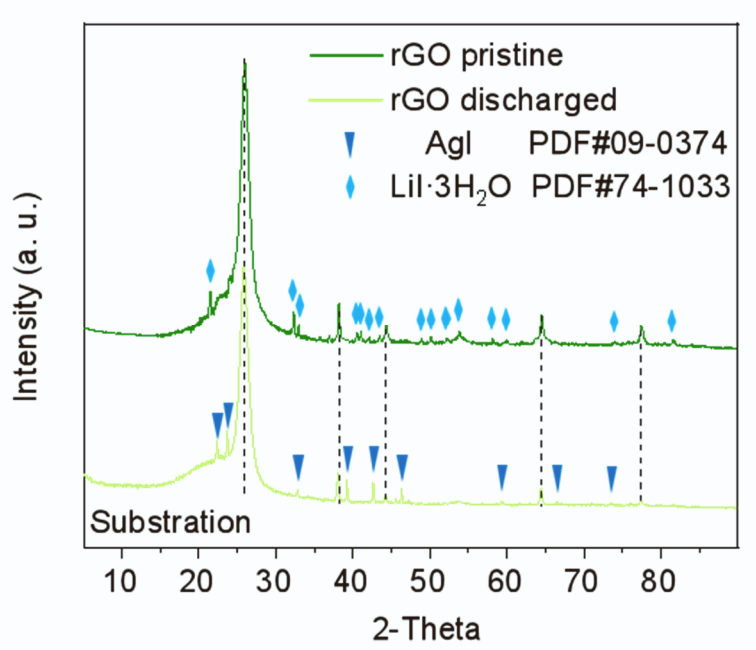

Figure S15. Characteristics of the rGO side before and after discharge.

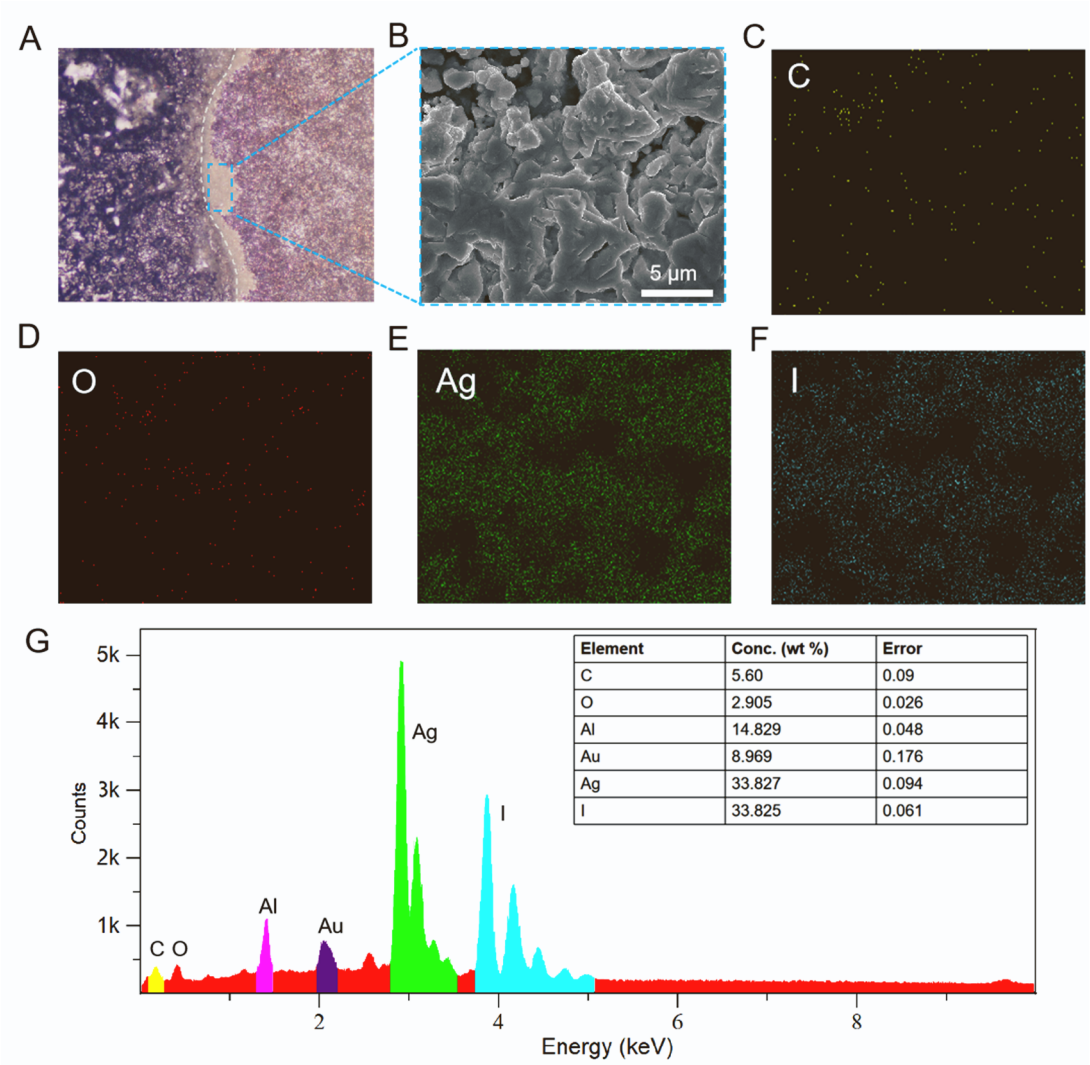

Figure S16. Characterization of the rGO anode side after discharge. (A) Optical photographs of the rGO on discharged Ag/$AgNO_3$-GO/LiI-rGO/Ag iontronic power source. **(B)** SEM image of the newly formed white crystals on rGO side. **(C-F)**Corresponding EDX mapping images on the discharged rGO for (C) C; (D) O; (E) Ag; (F) I. **(G)** EDX of the newly formed white crystals, showing a mass ratio of Ag to I elements of 1:1, as expected for the oxidation of Ag to Ag^+ combined with I^-.

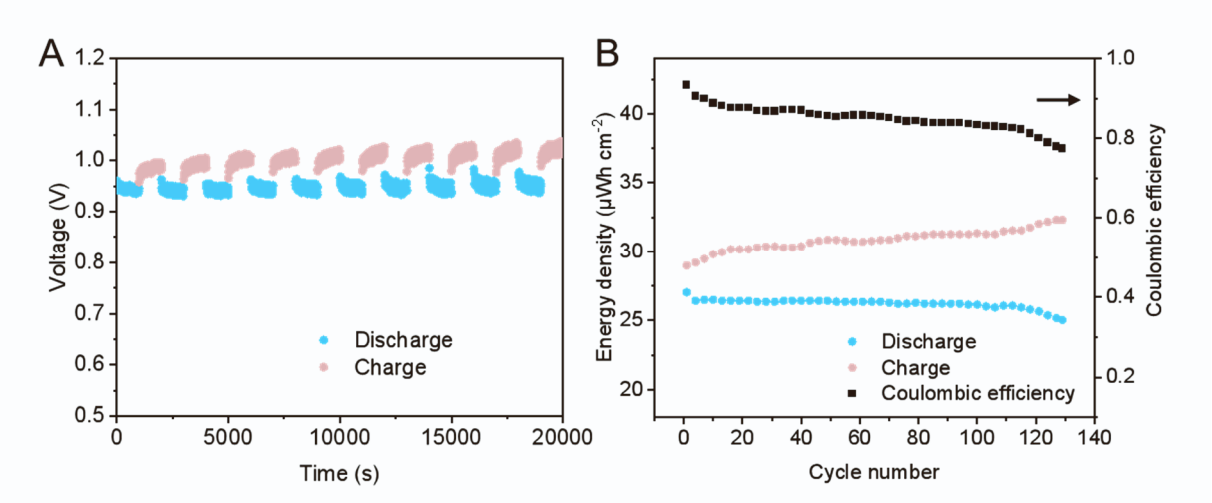

Figure S17. Cycling test. (A) Charging and discharging tests of the first ten cycles were performed on iontronic power source at intervals due to its stable voltage plateau, which makes it difficult to set the voltage to predict its discharge endpoint. **(B)** cycling stability and Coulombic efficiency tests of the iontronics.

In addition, the cost-effective manufacturing process of our printable iontronic power source make it perfect primary battery for disposable electronics.

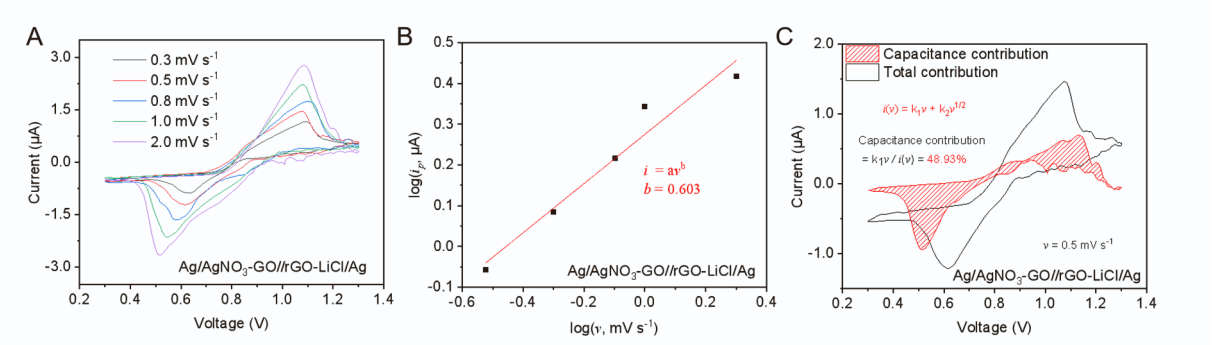

Figure S18. Iontronic interfacial dynamics of the Ag/AgNO$_3$-GO//rGO-LiCl/Ag. (A) CV test at different voltage scan rate from 0.3 mV s^{-1} to 1.3 mV s^{-1}. **(B)** Corresponding log(i_p) versus log(v), and the calculated b value is 0.603. **(C)** Estimation of diffusion capacitance by pseudocapacitance method at 0.5 mV s^{-1} and the contribution of the capacitance is 48.93%.

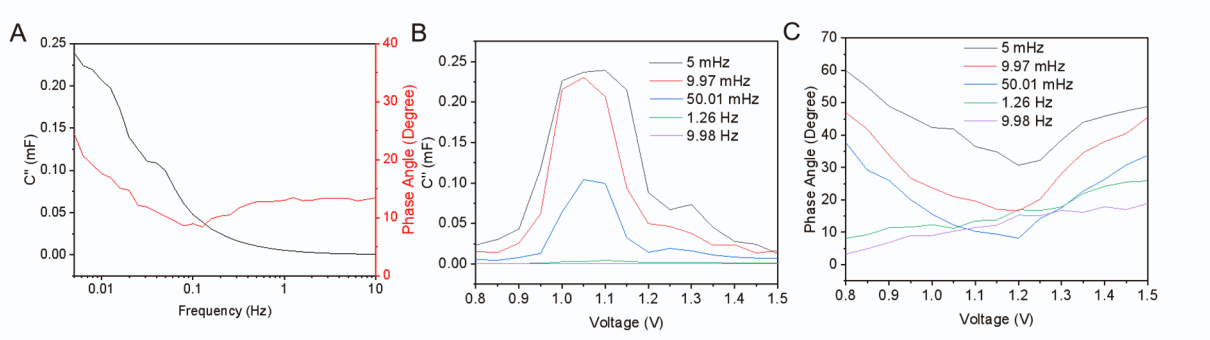

Figure S19. 2D Bode for Interfacial ion dynamics (A) 2D Bode plots in the form of the real capacitance and phase angle vs frequency. **(B-C)** 2D plots in the form of the real capacitance (B) and phase angle (C) vs voltage.

2D Bode plot (Figure S19A) at half-wave potential ($E_{1/2}$) firstly showed the C' was 0.24 mF at low frequency of 5 mHz, which means the redox processes took place, thus giving rise to high capacitance [8]. Figure S19A also shown a tendency of increasing φ values in the high and low frequency regions, indicating the capacitive behaviors [9]. The negative dependence between φ and C′ was depicted in Figure S19B-C at low frequencies in the same tendency of voltages, φ and C′ were almost stable at higher frequencies (1.26 Hz and 9.98 Hz), indicative of a resistive process [9]. Yet, the high C′ values and the surface-controlled kinetics determined from CV analyses (Figure 4A) show a highly intricate pseudocapacitance process.

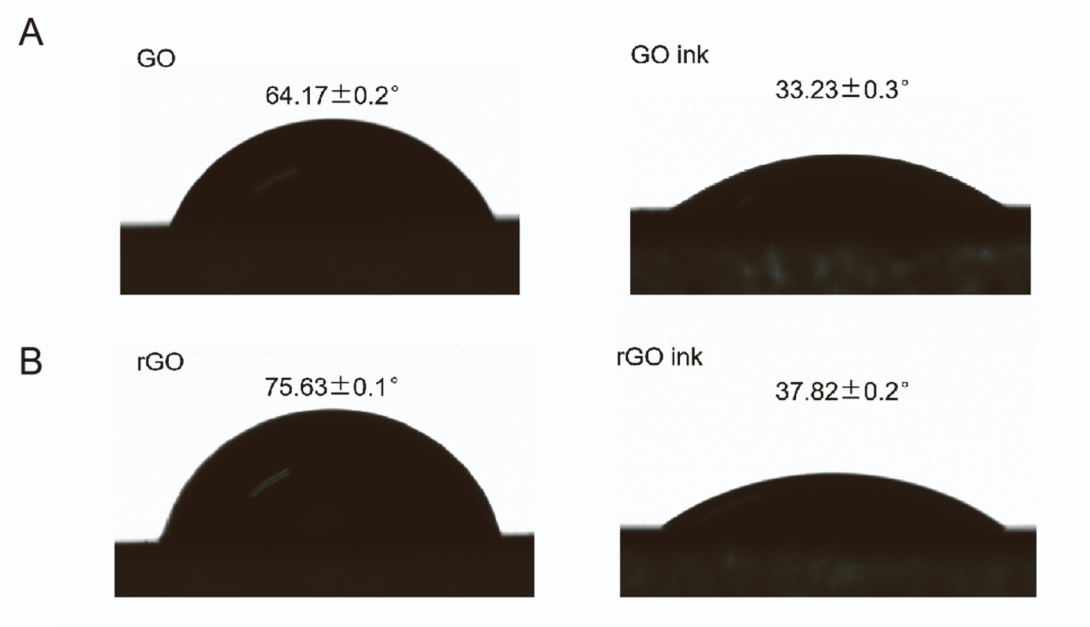

Figure S20. Contact angle measurements of GO and rGO inks on Ag substrate. (A) With the addition of Nafion, the contact angle of GO has changed from 64.17° to 33.23°. **(B)** With the addition of SDS, the contact angle of rGO has changed from 75.63° to 37.82°.

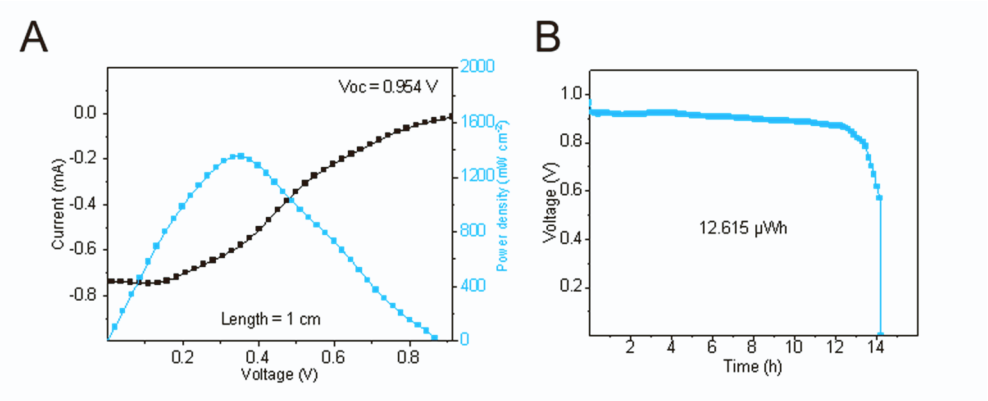

Figure S21. Corresponding electrochemical characterizations of the printed iontronics. **(A)** I-V characteristics and **(B)** The discharge curve of the Ag/$AgNO_3$-GO-Nafion/LiI-rGO-SDS/Ag iontronic power source, demonstrating the addition of surfactant did not affect much of its electrical properties.

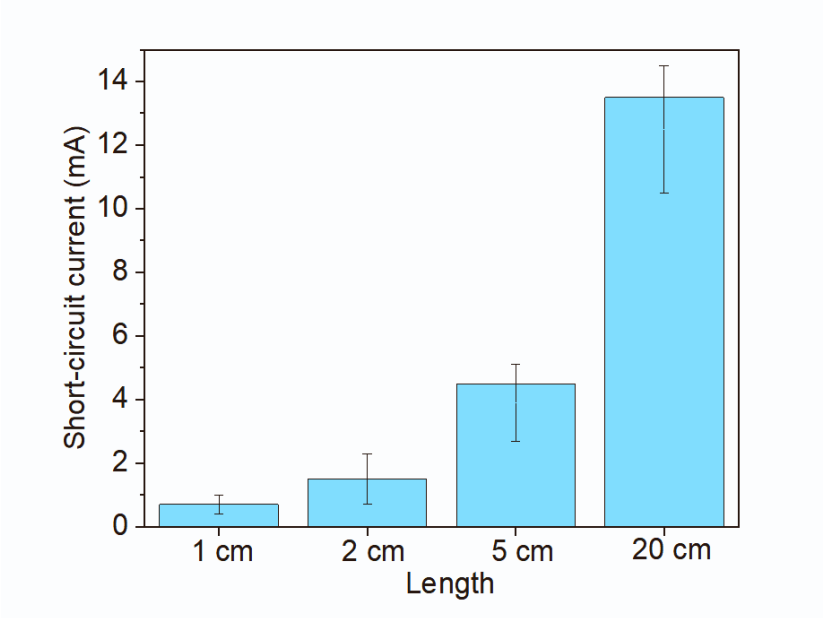

Figure S22. The influence of printing length on the iontronic power source. Histograms showing the relationship of Isc with different length of the printed iontronic power source.

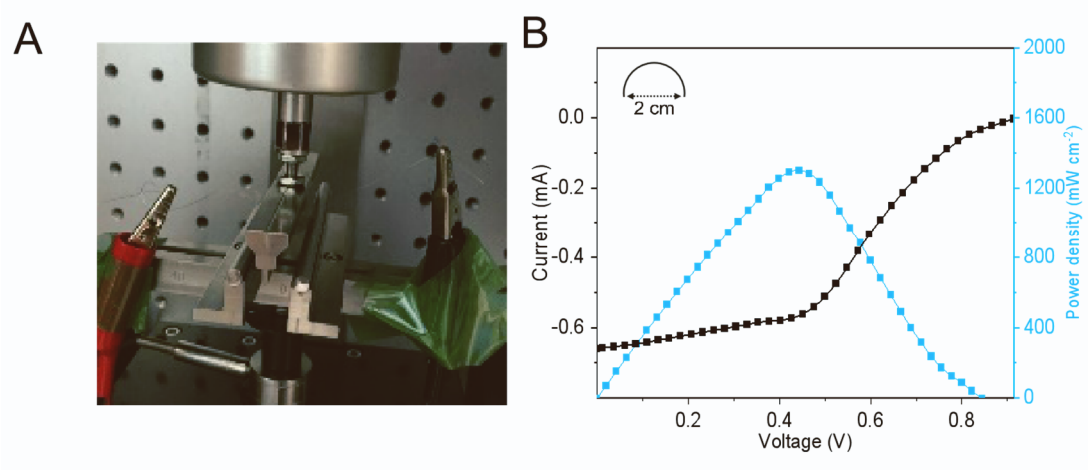

Figure S23. Bending test of the iontronic power source. (A) Bending fatigue test under a bending radius of ~1 cm. **(B)** Corresponding I-V characteristics.

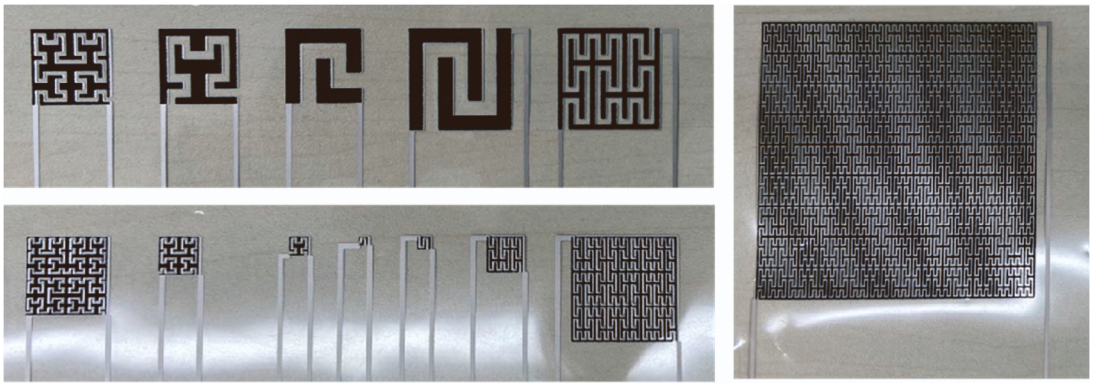

Figure S24. The printable fractal designed electrodes.

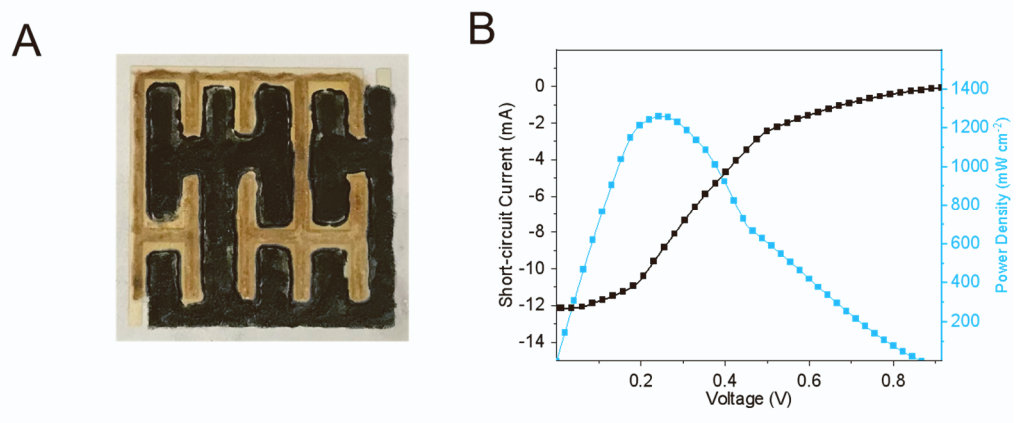

Figure S25. Printable iontronic power source with fractal design. (A) Picture of the iontronic power source with the pattern of Peano curves. **(B)** corresponding I-V characteristics.

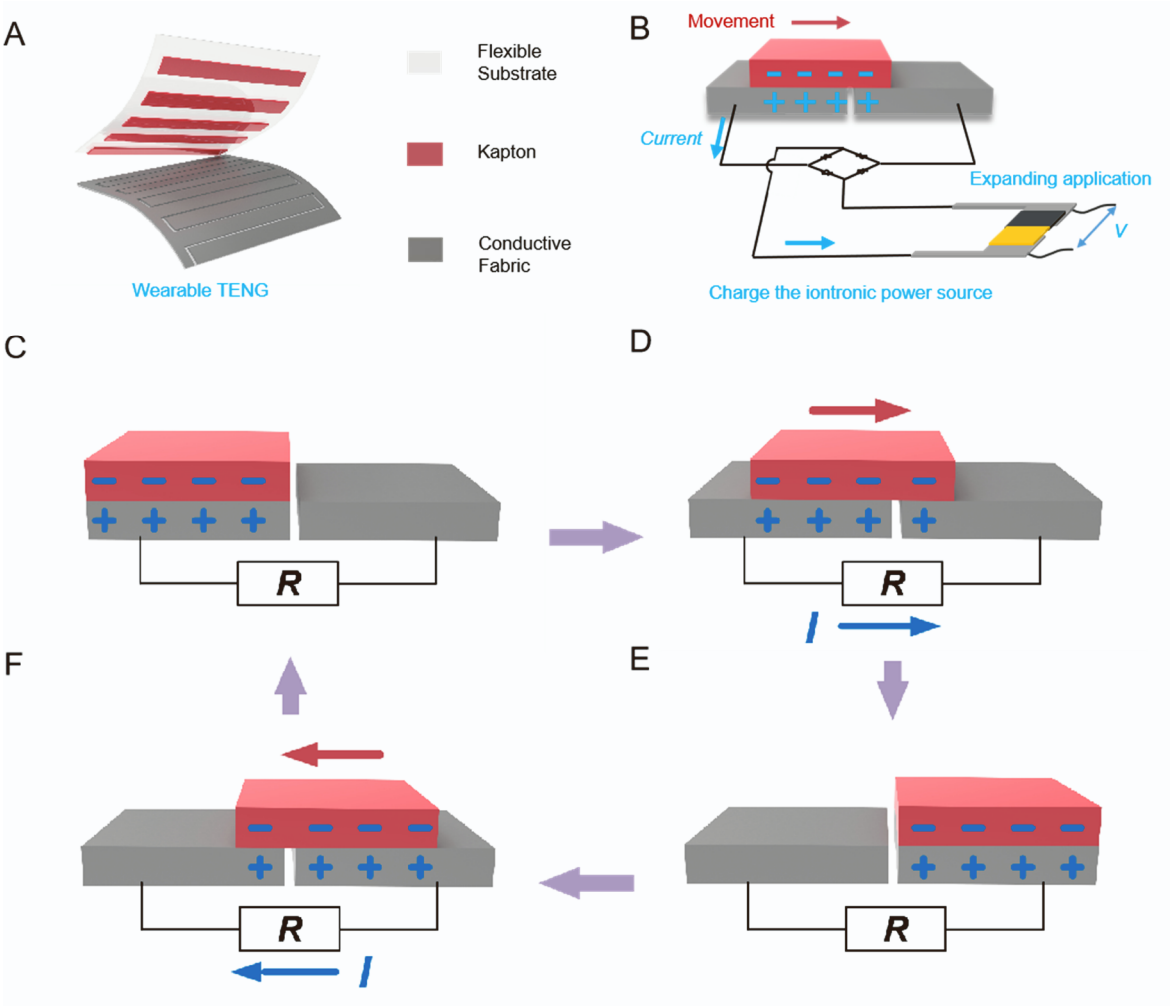

Figure S26. Triboiontronic device and the working mechanism. (A) Schematic of the energy harvesting structure of F-TENG. **(B)** Schematic of the integrated F-TENG with iontronic power source. **(C-E)** Based on the coupling effect of contact electrification and electrostatic induction, the F-TENG could generate triboelectric potential and displacement current to power the power source. In F-TENG, two pieces of conductive fabric intersecting each other were used as electrode layers, and Kapton material was used as an independent friction layer. The structure design of this freestanding triboelectric-layer mode TENG enables the electrode layer and friction layer independent of each other.

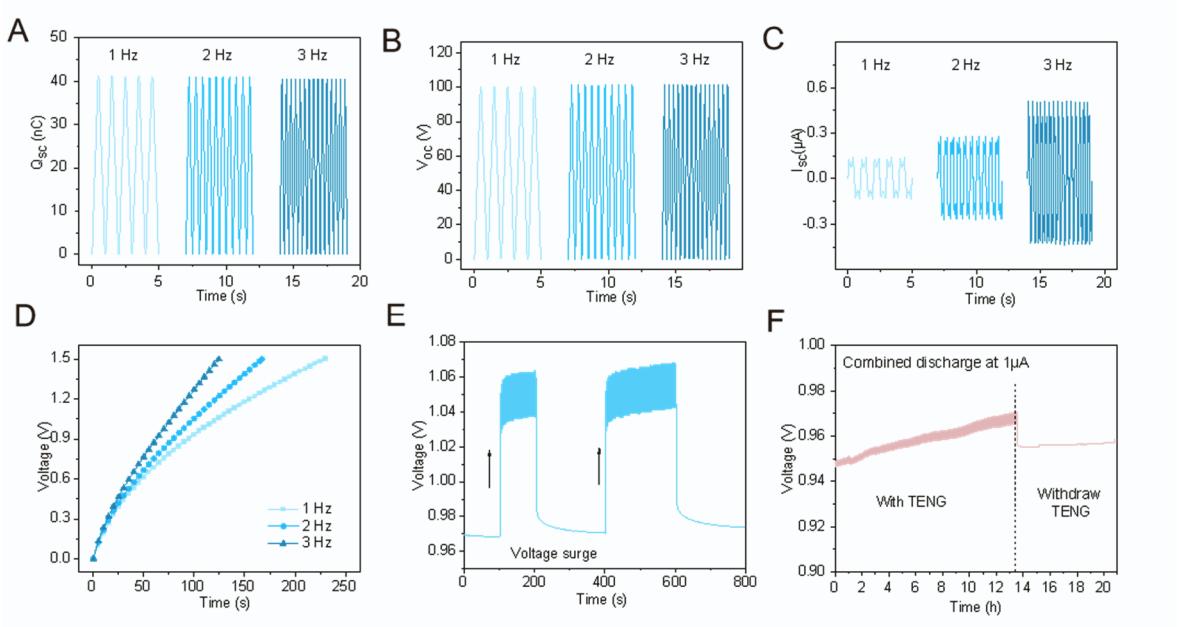

Figure S27. Performance of the conformable Self-charging Triboiontronics. (A) The output of charge, **(B)** open circuit voltage and **(C)** short circuit current at different frequencies. **(D)** Charging a capacitor (22 μF) by the F-TENG at different frequencies. **(E)** The chronopotential test of Ag/$AgNO_3$-GO/LiI-rGO/Ag power source charged by the F-TENG at 3 Hz. **(F)** The galvanostatic discharge performance of Ag/$AgNO_3$-GO/LiI-rGO/Ag integrated with F-TENG at 1 μA.

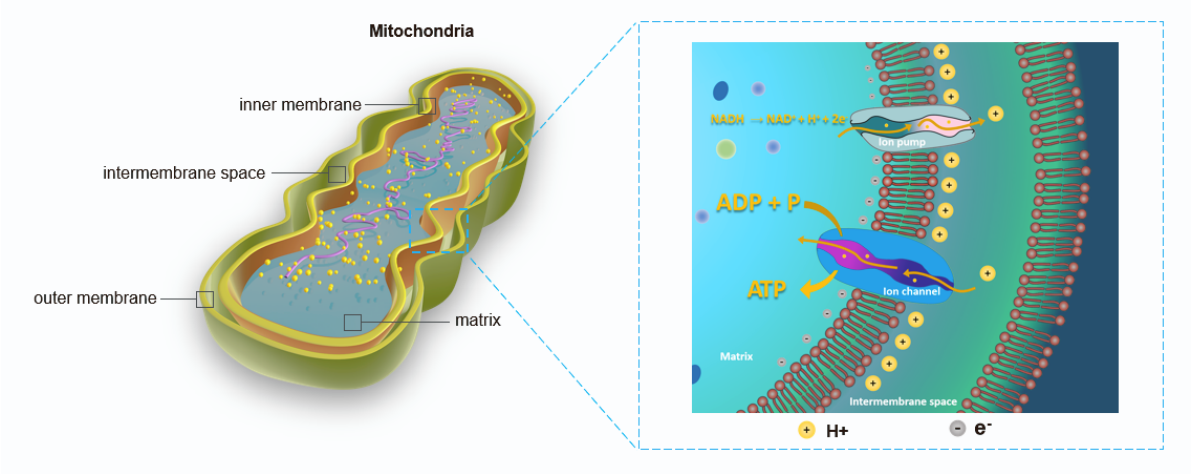

Figure S28. Schematic of the mechanism of chemiosmotic coupling in mitochondria. The pattern on the left shows a schematic of the internal structure of a mitochondria, which is surrounded by two biological membranes with many elaborate ion exchange channels. The diagram on the right shows a complete conversion of ADP to ATP. NADH obtained from external chemicals would be oxidatively decomposed to produce electrons, and the energy of those electrons will transfer the hydrogen ion pump in the membrane to send the H^+ from the inside of the membrane to the membrane gap, creating a concentration gradient of H^+. At the same time, H^+ would be transported back by passive transport, i.e. osmosis, in the membrane's ion channels, this process is thought to generate osmotic energy to induce the bonding of ADP and phosphate groups in the mitochondria, resulting in the production of ATP.

Table S1. Comparison of the areal output from various power sources.

Type	Materials	Power density ($W\ m^{-2}$)	Energy density ($Wh\ m^{-2}$)	Ref
This work	Redox in GO nanoconfined channels	16071.4	1391.6	
Iontronics	GO/rGO hydrogel	168	36	[10]
	GO film	2	20	[11]
	GO/rGO junction	1.5	1.1	[12]
	GO membrane pairs	0.77	N/A	[13]
	GO Van der Waals crystal	5.26	~802.6	[14]
	MXene/Kevlar nanofiber	4.1	over 28.8	[15]
	covalent organic framework monolayer	203.8	Over 509.5	[16]
	MoS_2 nanopores	10^6	N/A	[17]
	individual double-walled carbon nanotube	22500	N/A	[18]
Batteries	Li–Si battery	5047.25	1170	[19]
	CNTs@TiN-TiO_2 Li–S	~791.3	~250.1	[20]
	S@graphene Li-S	198.9	166.9	[21]
	Polymer Zn^{2+} battery	~1536.06	~67.92	[22]
	MWCNT/V_2O_5 LIB	216.35	8.4	[23]
	LCO LIB	50.32	74.98	[24]
	LTO LIB	78.67	25.9	[24]
	Zn-Ni battery	439.5	6.77	[25]
	Ni-Fe battery	524.45	4.4	[26]
	S@C Li-S	29.79	98.84	[27]
	C@S Li-S	517.16	42.67	[28]
	Ag-Zn battery	22.92	44.73	[29]
	Li^+ thin film	~21.83	~20.08	[30]
Supercapacitor	Carbon onions	~9432.6	~1.57	[30]
	Wood carbons	248.3	4.8	[31]
	Metal silicates	3.8	3.2	[32]
	C@Co, CoO/Co_2SiO_4/rGO	1.5	1.373	[33]
	$Co(OH)_2$@CoF	2355	198.3	[34]
	Cobalt-nickel silicate hydroxide/C	3.75	0.793	[35]

N/A, not available.

Supplemental reference:

1. Bard, A. J. and Faulkner, L. R. (2001). Electrochemical Methods: Fundamentals and Applications. New York, Second ed. (John Wiley & Sons, Inc.).
2. Esfandiar, A., Radha, B., Wang, F. C., Yang, Q., Hu, S., Garaj, S., Nair, R. R., Geim, A. K. and Gopinadhan, K. (2017). Size effect in ion transport through angstrom-scale slits. Science (New York, N.Y.) 358, 511-513. 10.1126/science.aan5275.
3. Yang, Q., Sun, P. Z., Fumagalli, L., Stebunov, Y. V., Haigh, S. J., Zhou, Z. W., Grigorieva, I. V., Wang, F. C. and Geim, A. K. (2020). Capillary condensation under atomic-scale confinement. Nature 588, 250-253. 10.1038/s41586-020-2978-1.
4. Qian, H., Wei, D. and Wang, Z. (2023). Bionic iontronics based on nano-confined structures. Nano Res. 16, 11718-11730. 10.1007/s12274-023-5705-z.
5. Wang, F., Jiang, C., Tang, C., Bi, S., Wang, Q., Du, D. and Song, J. (2016). High output nano-energy cell with piezoelectric nanogenerator and porous supercapacitor dual functions – A technique to provide sustaining power by harvesting intermittent mechanical energy from surroundings. Nano Energy 21, 209-216. 10.1016/j.nanoen.2016.01.018.
6. Cheng, X., Tang, W., Song, Y., Chen, H., Zhang, H. and Wang, Z. L. (2019). Power management and effective energy storage of pulsed output from triboelectric nanogenerator. Nano Energy 61, 517-532. 10.1016/j.nanoen.2019.04.096.
7. Eriksson, H. A. S. (1937). Ionization Energy of Li+ and He. Nature 140, 151-151. 10.1038/140151a0.
8. Wu, P., Wu, J., Si, H., Zhang, Z., Liao, Q., Wang, X., Dai, F., Ammarah, K., Kang, Z. and Zhang, Y. (2020). 3D Holey-Graphene Architecture Expedites Ion Transport Kinetics to Push the OER Performance. Adv. Energy Mater. 10, 10.1002/aenm.202001005.
9. Ko, J. S., Lai, C.-H., Long, J. W., Rolison, D. R., Dunn, B. and Nelson, W. J. (2020). Differentiating Double-Layer, Psuedocapacitance, and Battery-like Mechanisms by Analyzing Impedance Measurements in Three Dimensions. ACS Appl. Mater. Inter. 12, 14071-14078. 10.1021/acsami.0c02020.
10. Wei, D., Yang, F., Jiang, Z. and Wang, Z. (2022). Flexible iontronics based on 2D nanofluidic material. Nat. Commun. 13, 4965. 10.1038/s41467-022-32699-x.
11. Wei, D. (2015). Writable electrochemical energy source based on graphene oxide. Sci. Rep. 5, 15173. 10.1038/srep15173.
12. Yang, L., Yang, F., Liu, X., Li, K., Zhou, Y., Wang, Y., Yu, T., Zhong, M., Xu, X., Zhang, L. et al. (2021). A moisture-enabled fully printable power source inspired by electric eels. Proc. Natl. Acad. Sci. U.S.A. 118, 10.1073/pnas.2023164118.
13. Ji, J., Kang, Q., Zhou, Y., Feng, Y., Chen, X., Yuan, J., Guo, W., Wei, Y. and Jiang, L. (2017). Osmotic Power Generation with Positively and Negatively Charged 2D Nanofluidic Membrane Pairs. Adv. Funct. Mater. 27, 10.1002/adfm.201603623.
14. Kim, S., Choi, S., Lee, H. G., Jin, D., Kim, G., Kim, T., Lee, J. S. and Shim, W. (2021). Neuromorphic van der Waals crystals for substantial energy generation. Nat. Commun. 12, 47. 10.1038/s41467-020-20296-9.
15. Zhang, Z., Yang, S., Zhang, P., Zhang, J., Chen, G. and Feng, X. (2019). Mechanically strong MXene/Kevlar nanofiber composite membranes as high-performance nanofluidic osmotic power generators. Nat. Commun. 10, 2920. 10.1038/s41467-019-10885-8.
16. Yang, J., Tu, B., Zhang, G., Liu, P., Hu, K., Wang, J., Yan, Z., Huang, Z., Fang, M., Hou, J. et al. (2022). Advancing osmotic power generation by covalent organic framework monolayer. Nat. Nanotechnol. 17, 622-628. 10.1038/s41565-022-01110-7.

17. Feng, J., Graf, M., Liu, K., Ovchinnikov, D., Dumcenco, D., Heiranian, M., Nandigana, V., Aluru, N. R., Kis, A. and Radenovic, A. (2016). Single-layer MoS2 nanopores as nanopower generators. Nature 536, 197-200. 10.1038/nature18593.
18. Cui, G., Xu, Z., Li, H., Zhang, S., Xu, L., Siria, A. and Ma, M. (2023). Enhanced osmotic transport in individual double-walled carbon nanotube. Nat. Commun. 14, 2295. 10.1038/s41467-023-37970-3.
19. Yan, W., Mu, Z., Wang, Z., Huang, Y., Wu, D., Lu, P., Lu, J., Xu, J., Wu, Y., Ma, T. et al. (2023). Hard-carbon-stabilized Li–Si anodes for high-performance all-solid-state Li-ion batteries. Nat. Energy 10.1038/s41560-023-01279-8.
20. Zhang, H., Ono, L. K., Tong, G., Liu, Y. and Qi, Y. (2021). Long-life lithium-sulfur batteries with high areal capacity based on coaxial CNTs@TiN-TiO_2 sponge. Nat. Commun. 12, 4738. 10.1038/s41467-021-24976-y.
21. Zhou, G., Li, L., Ma, C., Wang, S., Shi, Y., Koratkar, N., Ren, W., Li, F. and Cheng, H.-M. (2015). A graphene foam electrode with high sulfur loading for flexible and high energy Li-S batteries. Nano Energy 11, 356-365. 10.1016/j.nanoen.2014.11.025.
22. Li, H., Han, C., Huang, Y., Huang, Y., Zhu, M., Pei, Z., Xue, Q., Wang, Z., Liu, Z., Tang, Z. et al. (2018). An extremely safe and wearable solid-state zinc ion battery based on a hierarchical structured polymer electrolyte. Energy Environ. Sci. 11, 941-951. 10.1039/c7ee03232c.
23. Chen, X., Zhu, H., Chen, Y.-C., Shang, Y., Cao, A., Hu, L. and Rubloff, G. W. (2012). MWCNT/V2O5 core/shell sponge for high areal capacity and power density Li-ion cathodes. ACS nano 6, 7948-55. 10.1021/nn302417x.
24. Gaikwad, A. M., Khau, B. V., Davies, G., Hertzberg, B., Steingart, D. A. and Arias, A. C. (2015). A High Areal Capacity Flexible Lithium-Ion Battery with a Strain-Compliant Design. Adv. Energy Mater. 5, 10.1002/aenm.201401389.
25. Liu, J., Guan, C., Zhou, C., Fan, Z., Ke, Q., Zhang, G., Liu, C. and Wang, J. (2016). A Flexible Quasi-Solid-State Nickel-Zinc Battery with High Energy and Power Densities Based on 3D Electrode Design. Adv. Mater. 28, 8732-8739. 10.1002/adma.201603038.
26. Guan, C., Zhao, W., Hu, Y., Ke, Q., Li, X., Zhang, H. and Wang, J. (2016). High-Performance Flexible Solid-State Ni/Fe Battery Consisting of Metal Oxides Coated Carbon Cloth/Carbon Nanofiber Electrodes. Adv. Energy Mater. 6, 10.1002/aenm.201601034.
27. Lv, D., Zheng, J., Li, Q., Xie, X., Ferrara, S., Nie, Z., Mehdi, L. B., Browning, N. D., Zhang, J.-G., Graff, G. L. et al. (2015). High Energy Density Lithium-Sulfur Batteries: Challenges of Thick Sulfur Cathodes. Adv. Energy Mater. 5, 10.1002/aenm.201402290.
28. Zhou, G., Zhao, Y. and Manthiram, A. (2015). Dual-Confined Flexible Sulfur Cathodes Encapsulated in Nitrogen-Doped Double-Shelled Hollow Carbon Spheres and Wrapped with Graphene for Li-S Batteries. Adv. Energy Mater. 5, 10.1002/aenm.201402263.
29. Braam, K. T., Volkman, S. K. and Subramanian, V. (2012). Characterization and optimization of a printed, primary silver–zinc battery. J. Power Sources 199, 367-372. 10.1016/j.jpowsour.2011.09.076.
30. Pech, D., Brunet, M., Durou, H., Huang, P., Mochalin, V., Gogotsi, Y., Taberna, P.-L. and Simon, P. (2010). Ultrahigh-power micrometre-sized supercapacitors based on onion-like carbon. Nat. Nanotechnol. 5, 651-4. 10.1038/nnano.2010.162.
31. Song, P., Chen, C., Shen, X., Zeng, S., Premlatha, S., Ji, Z., Zhai, L., Yuan, A. and Liu, Q. (2022). Metal-organic frameworks-derived carbon modified wood carbon monoliths as three-dimensional self-supported electrodes with boosted electrochemical energy storage performance. J. Colloid Interface Sci. 620, 376-387. 10.1016/j.jcis.2022.04.048.

32. Zhang, Y., Wang, C., Dong, X., Jiang, H., Hu, T., Meng, C. and Huang, C. (2021). Alkali etching metal silicates derived from bamboo leaves with enhanced electrochemical properties for solid-state hybrid supercapacitors. Chem. Eng. J. 417, 10.1016/j.cej.2020.127964.
33. Dong, X., Jing, X., Mu, Y., Yu, Y., Miao, C., Meng, C., Huang, C. and Zhang, Y. (2022). Rational design of double-sandwich-like C@Co,CoO/Co2SiO4/rGO architectures boost electrochemical performances of Co2SiO4 for energy storage devices. Chem. Eng. J. 431, 10.1016/j.cej.2021.133277.
34. Fan, Y., Wang, L., Huang, W., Dong, Y., Ma, Z., Guo, W. and Mai, L. (2019). Co(OH)2@Co electrode for efficient alkaline anode based on Co2+/Co° redox mechanism. Energy Stor. Mater. 21, 372-377. 10.1016/j.ensm.2018.12.008.
35. Zhang, Y., Wang, C., Jiang, H., Wang, Q., Zheng, J. and Meng, C. (2019). Cobalt-nickel silicate hydroxide on amorphous carbon derived from bamboo leaves for hybrid supercapacitors. Chem. Eng. J. 375, 10.1016/j.cej.2019.121938.